Journal of Materials Chemistry A

ROYAL SOCIETY OF CHEMISTRY

REVIEW

View Article Online
View Journal | View Issue

Cite this: J. Mater. Chem. A, 2024, 12, 23125

Latest advances in *in situ* and *operando* X-ray-based techniques for the characterisation of photoelectrocatalytic systems

Mariam Barawi, [a] Camilo A. Mesa, [b] Laura Collado, [a] Ignacio J. Villar-García,[c] Freddy Oropeza, [a] Víctor A. de la Peña O'Shea *[a] and Miguel García-Tecedor *[a]

In situ and *operando* X-ray techniques have emerged as powerful tools for unravelling the complex mechanisms underlying photoelectrochemical transformations. These techniques offer real-time insights into the dynamic processes occurring at the electrode–electrolyte interface during solar-driven water splitting and other PEC reactions. The present work aims to summarise the latest advances in *in situ* and *operando* X-ray absorption spectroscopy (XAS), X-ray diffraction (XRD), and X-ray photoelectron spectroscopy (XPS) for the characterisation of photoelectrocatalytic systems and materials for the generation of solar fuels and value-added chemicals. This review highlights the recent advancements achieved using these techniques for elucidating the structural, chemical, and electronic properties of photoelectrocatalytic materials and interfaces during operation. Besides, this review provides technical guidance for performing these measurements, considering the experimental requirements for each of these spectroscopies. Further, we provide an overview of different state-of-the-art synchrotron-based techniques employed for the characterisation of photoelectrocatalytic materials, focusing on the possibilities of the studied techniques, cell designs and more relevant results.

Received 3rd May 2024
Accepted 19th July 2024

DOI: 10.1039/d4ta03068k

rsc.li/materials-a

Introduction

Artificial photosynthesis technologies have been attracting increasing attention, from fundamental understanding to, more recently, the industry, as an alternative source of fuels and value-added chemicals using ubiquitous molecules, such as CO_2 and H_2O, and sunlight.[1–3] These technologies have achieved higher technology readiness levels (TRLs) of development

[a]Photoactivated Processes Unit, IMDEA Energy, Avda. Ramón de la Sagra, 3, Móstoles, 28935, Spain. E-mail: miguel.tecedor@imdea.org; victor.delapenya@imdea.org
[b]Catalan Institute of Nanoscience and Nanotechnology (ICN2), CSIC, Barcelona Institute of Science and Technology, UAB Campus, 08193 Bellaterra, Barcelona, Spain
[c]Department of Chemistry and Biochemistry, Facultad de Farmacia, Universidad San Pablo-CEU, CEU Universities, Boadilla del Monte, 28668 Madrid, Spain

Miguel García-Tecedor

Miguel García Tecedor (PhD in Physics 2017, Universidad Complutense de Madrid) is a Senior Assistant Researcher at IMDEA Energy. During his PhD, he was focused on the growth and characterisation of semiconducting nanostructures and their applications in optoelectronics and energy. As part of his international PhD, in 2015, he joined the Institute for Energy Technology, located in Kjeller, Norway, to work on the synthesis and characterisation of organic–inorganic composites for silicon solar cells' passivation. In July 2017, he took a position as Research Scientist at the Institute of Advanced Materials at Universitat Jaume I, to develop novel strategies for (photo)electrocatalytic water splitting and CO_2 reduction. Lately, in March 2021, Miguel joined the Photoactivated Processes Unit at IMDEA Energy to work on photo(electro)catalytic approaches towards wastewater oxidation, CO_2 reduction and N_2 fixation. Miguel is currently co-author of 45 scientific publications and he has participated in 14 research projects, being principal investigator in three.

in recent years, and are becoming a real alternative for the generation of solar fuels and chemicals at an industrial level. In the case of photoelectrochemical (PEC) routes, different architectures could be considered: (i) full photoelectrochemical systems, where both anode and cathode contain photoabsorber materials, (ii) electrocatalytic systems coupled to photovoltaic cells (PV-EC) and (iii) photoelectrochemical systems coupled to photovoltaic cells to reduce the overpotential for the target chemical reaction.[4] In recent years, all these technologies have increased their maturity towards industrialisation. As explained in the recent work by G. Segev *et al.*,[5] lab-scale photoelectrochemical devices exhibit efficiencies over 10% currently, which has been traditionally considered as the minimum threshold for any industrial application. However, in order to establish the photoelectrocatalytic approach at a relevant industrial level, from both the scientific and economic points of view, there are still many technological questions to be answered and physicochemical mechanisms to be revealed. To overcome this problem, the scientific community is currently highly interested in *operando* and *in situ* methods, which allow for the characterisation of the photoelectrocatalytic materials under relevant working conditions.[6,7]

In particular, "*in situ*" characterization refers to the study of materials, usually catalysts, and reactions in their natural working environment without disrupting the experimental conditions. It is performed within the reactor or reaction cell during the reaction but not necessarily under real operating conditions. However, "*operando*" characterization refers to the study of materials and catalytic reactions under real operating conditions. Both approaches are crucial for understanding and improving the catalytic systems; however, they are applied in slightly different contexts depending on whether a study is needed under controlled conditions (*in situ*) or realistic catalytic conditions (*operando*).[8]

Spectroscopy-based techniques are powerful tools to investigate the photoelectrode–electrolyte interface where information on the electronic and structural nature of the active sites can be obtained upon careful selection of excitation and probe sources.[9] As such, there is a growing tendency in the field to perform an *in situ* and *operando* analysis using various techniques such as Raman spectroscopy,[10,11] UV-vis spectroscopy,[12] Fourier-transform infrared (FTIR) spectroscopy,[13] electrochemical impedance spectroscopy (EIS),[14] and incident modulated photocurrent spectroscopy (IMPS),[15] due to the key importance of understanding the materials under real working conditions. Hence, the combination of *in situ* and *operando* synchrotron techniques with photoelectrocatalytic experiments is pivotal to understand the performance of these materials, in terms of stability, efficiency, and selectivity, under working conditions and thus, establishing this technology as an important element in the green energy transition.

In terms of X-ray-based spectroscopy techniques such as XPS, XAS and XRD, the majority of *in situ* and *operando* reported PEC studies have employed synchrotron radiation. This is due to the advantages of synchrotron radiation compared with other lab-scale X-ray sources: (i) high brightness and energy resolution, which enables high-speed data acquisition and provides more accurate data, (ii) high spatial resolution, which allows for precise material mapping, (iii) wide energy range, enabling variable energy X-ray techniques (XAS) and conducting experiments at a range of selected optimum wavelengths (XPS and XRD), (iv) polarized nature, allowing specific experiments to probe the magnetic and electronic properties of materials and (v) precise flashing time structure at a very high frequency, which can be used to study physical and chemical processes taking place at very short time scales.[16]

In situ and *operando* synchrotron techniques are more mature in the electrocatalytic (EC) field, which can be explained not only by the maturity of the field but also due to several inherent difficulties in order to study photoelectrocatalytic reactions *in situ*: (i) although many novel oxide and chalcogenide electrocatalysts undergo bulk changes that lead to the actual catalytic species,[17–20] the bulk of photoelectrodes are usually stable and most relevant changes are limited to their surfaces involving usually a few tens of nanometres,[21,22] which demands surface-sensitive techniques or special analysis modes to make commonly bulk techniques surface sensitive, and both (ii) the need to illuminate the sample during operation,[23] and (iii) the usual employment of thick transparent conductive substrates (FTO or ITO, most frequently), instead of thin current collectors, add an extra level of complexity to the experimental set-up. Due to these challenges, only a few works have reported successful *in situ* or *operando* synchrotron-based spectroscopies in photoelectrochemical systems.

This review aims to give a general vision of the current state of the art of *in situ* and *operando* X-ray-based studies, focusing mainly on X-ray photoelectron spectroscopy (XPS), X-ray absorption spectroscopy (XAS) and X-ray diffraction spectroscopy (XRD), in PEC systems for solar fuel generation (Scheme 1). Besides, this work provides technical guidance for performing these experiments at synchrotron facilities, with the hope of increasing the activity in this field, which has the potential to answer some of the main questions to take the comprehension of PEC systems to the next level.

By synthesizing and critically evaluating these analytical possibilities, this work aims to serve as a pivotal resource for guiding future research efforts and informing the design of more efficient and sustainable photoelectrocatalytic technologies. We believe that the comprehensive nature of this revision, its clear organization of existing knowledge, and its potential to advance the field make it well-suited for energy researchers interested in initiating or advancing their work with *operando* and *in situ* experiments in PEC systems.

In situ and *operando* X-ray photoelectron spectroscopy (XPS)

X-ray photoelectron spectroscopy (XPS) is a commonly used characterisation technique for the analysis of the surface of materials. This technique, also called ESCA (Electron Spectroscopy for Chemical Analysis), provides qualitative and quantitative elemental analysis, except for hydrogen and helium, of the top 1–20 nm (depending on the sample and instrumental conditions) of a surface.[24] In XPS, the sample is irradiated with soft X-rays (energies lower than ~6 keV) and the

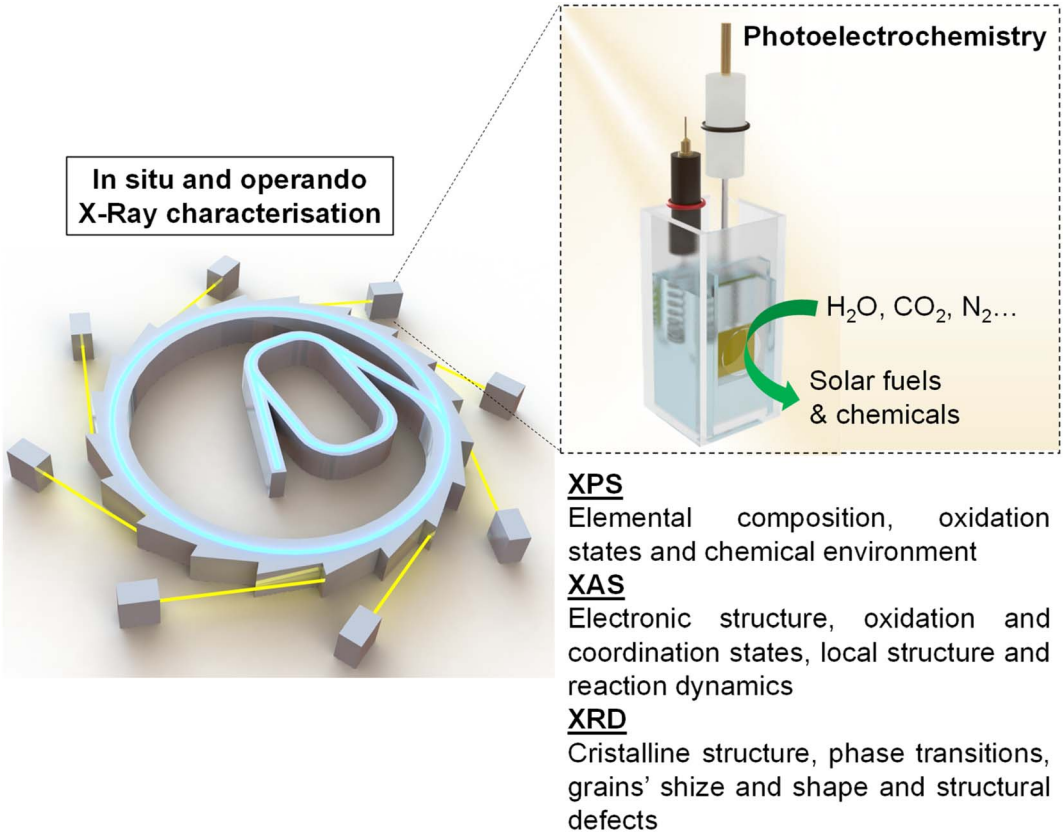

Scheme 1 Overview of the addressed topics in the present review.

kinetic energy of the emitted electrons is analysed. When an X-ray of known energy ($h\nu$) interacts with an atom, a photoelectron can be emitted *via* the photoelectric effect. The emitted photoelectron is the result of complete transfer of the X-ray energy to a core level electron. It simply states that the energy of the X-ray ($h\nu$) is equal to the binding energy (E_b) of the electron (how tightly it is bound to the atom/orbital to which it is attached) plus the kinetic energy (E_k) of the electron that is emitted and the spectrometer work function (Φ_{sp}), a constant value, and hence, E_b can be calculated using the following equation:

$$E_b = h\nu - E_k - \Phi_{sp} \quad (1)$$

Thus, valuable chemical information about the sample can be extracted because binding energies are sensitive to the chemical environment of the atom.[25] Hence, XPS provides unique information on the chemical composition and electronic structure of materials, so that it has been traditionally used for the fundamental characterisation of semiconductors with application in the field of photoelectrochemistry. The development of near-ambient pressure (NAP) XPS has extended the applications of XPS to the performance of detailed studies of the chemical state of photoelectrodes and the reaction intermediates under relevant or even *operando* conditions, which facilitate the understanding of reaction mechanisms. As a result, NAP XPS is nowadays commonly used for the *in situ* characterisation of catalytic, photocatalytic and (photo) electrocatalytic reactions. The field has evolved exponentially since the development of the new generation of NAP XPS analysers at the beginning of the century.[26] The last comprehensive review in 2020 estimates that there are more than 70 NAP XPS systems around the world, including laboratory and synchrotron-based systems.[27] Most NAP XPS systems allow the dosing of gases and gas mixtures and heating in order to perform *in situ* characterisation of heterogeneous catalytic reactions in different gas atmospheres. These systems can be easily adapted for electrochemical systems based on solid electrolytes.[28] However, the measurement of electrocatalytic systems based on liquid electrolytes requires the use of especially designed electrochemical cells.[29] There are two main types of approaches in the literature for the *operando* analysis of electrochemical reactions using liquid electrolytes by XPS. One requires the use of graphene windows that separate the liquid and UHV environments, and through which, X-rays and electrons can pass through, allowing XPS measurements. Despite being first established in 2011,[30] these cells have been rarely studied, mainly due to the fragility of these 2D windows under operation in UHV chambers.[31,32] The other approaches are windowless and require the delicate fine control of the continuous evaporation of the electrolyte in a UHV chamber.[33] which requires a fine balance of the operating conditions but has given rise to a more significant amount of contributions in both photoelectrochemical and electrocatalytic studies.[28]

The performance of *in situ* measurements of photoelectrocatalytic systems adds an additional complication to the photoelectrochemical approach, as the sample must be properly illuminated. For the illumination, there are two possibilities, direct illumination by the set-up of an UV light within the UHV chamber using electrical feedthroughs or illumination through a window outside the XPS instrument. This port can be one facing directly at the sample in the UHV chamber or the port at the photoelectron analyser that allows directing light down the axis of the spectrometer. Common UHV windows made of borosilicate allow the transmittance of most ultraviolet light down to 300/350 nm wavelengths. If the experiments require the use of more energetic UV radiation, UV windows made of sapphire, fused silica or even MgF_2 could be used with absorbance cut-offs that go down to 200 nm wavelengths.[34] Specifically, there are different available commercial windows for performing these experiments: (i) OROFLOAT borosilicate windows (Edmund Optics) have a transmission of more than 90% between 350 and 2500 nm; (ii) TECHSPEC sapphire windows (Edmund Optics) are useful in the transmission range of 330–5500 nm; (iii) fused quartz windows (Knight Optical) are a more suitable material choice for UV light; and (iv) any other window materials of the correct size, which satisfies the needs of the users' experiment. User-supplied light sources can also be attached to the main chamber with minimal effort. Moreover, illumination from outside the UHV chamber requires a lens focusing system at the sample distance or a large collimated source. This latter set up adds the advantage of illuminating the sample only in the area of investigation. One also has to consider that depending on the energy range and intensity, illumination can lead to sample heating. Therefore, a way to measure the temperature of the sample or a previous calibration is advisable, in order to discount the temperature effect on the studied reaction.

The dip and pull method, shown in Fig. 1, is probably the easier type of electrochemical cell to adapt to photoelectrocatalytic measurements and the method of choice in most photoelectrochemical studies reported in the literature. In particular, the SpAnTeX endstation at the BElChem-PGM endstation in BESSY II offers a dip and pull module specially designed for photoelectrocatalytic measurements.[35] Other end stations that offer the dip and pull method such as HIPPIE in Max IV, PHOENIX I at Swiss Light Source (SLS) or BL 9.3.1 at Advanced Light Source (ALS) could be easily adapted to photoelectrochemical experiments building up on their experience on photocatalytic reaction monitoring. Most of the dip and pull measurements are done in Synchrotron stations using tender X-rays (2–7 keV) as photoelectrons of high energy have more probabilities of going through the thin electrolyte meniscus that is created in order to allow electrons coming from the "buried" electrode to reach the analyser. As the probabilities of emitting photoelectrons of most probed orbitals go down significantly with excitation energy, 3 keV seems to be the sweet spot for maximising the signal intensity of the buried electrodes.[33] Nevertheless, experiments can be done at lower excitation energies, *e.g.* the HIPPIE beamline works at a maximum excitation energy of 2.2 keV and laboratory systems have also been used successfully to probe buried liquid interfaces in battery systems, for example.[36] Moreover, the use of silver (Ag Kα, 2.9 keV) or chromium (Cr Kα, 5.4 keV) sources can increase the probing depth of laboratory systems, complementing the experiments done with the typical Al Kα sources (1.5 keV). The added advantage of using synchrotron systems is that the variable energy can also be used to differentiate between surface and subsurface signals from the electrode, as surface signals

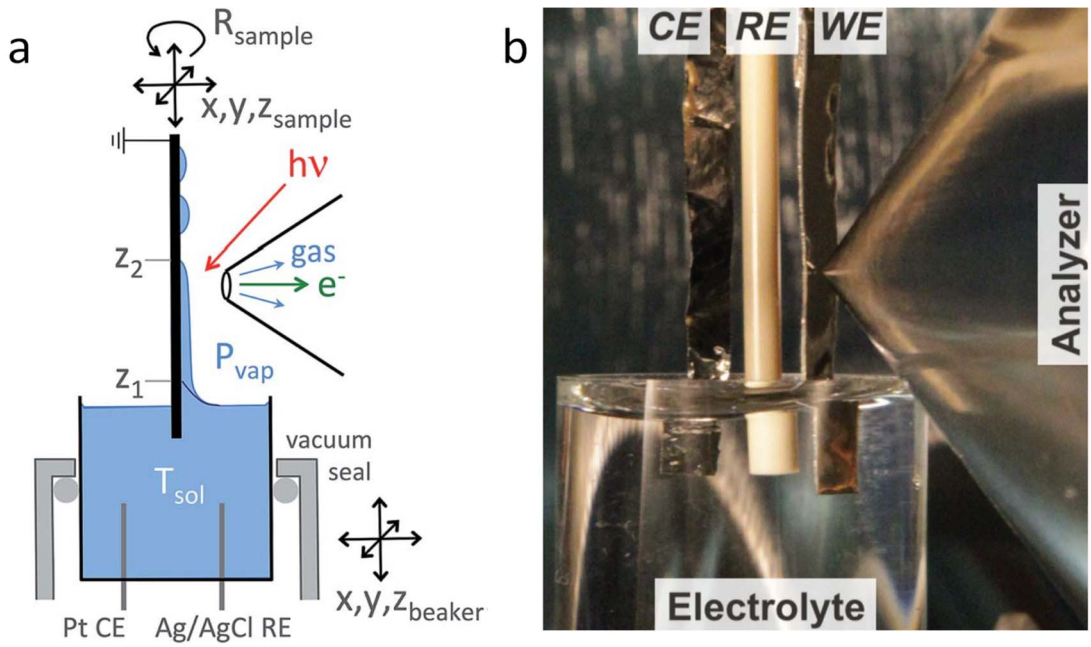

Fig. 1 (a) Scheme of the dip and pull method for the preparation of thin liquid films on electrodes. (b) Picture of the dip and pull set up at ALS. Copyright 2015. Reproduced with permission from Springer Nature. Adapted from ref. 33.

will be more enhanced at lower excitation energies. Moreover, synchrotron light allows performing Auger yield NEXAFS, which provides complementary surface-sensitive XAS information.

The possibility of performing *in situ* and *operando* XPS experiments using these setups has advanced the knowledge of the surface chemistry and electronic properties of photoabsorber materials that are used as photoelectrodes under real conditions of illumination and chemical environment. These studies can be divided into three categories based on how close to the actual *operando* conditions they are performed: (1) XPS under UV-visible illumination in UHV, (2) XPS under UV-visible illumination in NAP conditions, and (3) *operando* XPS. In the following subsections, we discuss these contributions in terms of the information obtained and the required facilities.

XPS of photoelectrodes under *in situ* illumination in UHV. Studying photoelectrodes using XPS under *in situ* illumination has helped in the elucidation of intrinsic light-induced changes of surface chemical states, electronic structures and the behaviour of charge carriers.[37] XPS has been particularly useful to study the surface photovoltage (SPV) of semiconductors used as photoelectrodes. The phenomenon of SPV arises from the distribution of photogenerated electron–hole pairs within the space charge region (SCR) of the semiconductor, providing a critical method for evaluating the minority carrier diffusion length in semiconductors. Since XPS is sensitive to changes in surface potential, this technique has been widely employed to carry out detailed SPV studies on organic and inorganic semiconducting materials.[38–40] This method, accessible through both synchrotron radiation and laboratory setups, simplifies the analysis of SPV by following shifts in photoemission peak positions under direct illumination. Early XPS-based SPV analyses were performed for Si(111) by Demuth *et al.*[38,41] finding that at temperatures below ~50 K, surface recombination becomes ineffective, thereby allowing flat-band conditions to be achieved with mild UV irradiation. Temperature-dependent photoemission thereby provides a simple and direct method for determining the band bending and barrier heights. XPS-based SPV measurement may be subject to artifacts due to charging, which motivated Suzer *et al.* to study dynamical XPS measurements for probing photoinduced voltage changes.[42] In order to distinguish between surface photovoltage (SPV), and charging, they proposed to perform dynamic measurements while subjecting the sample to square-wave pulses of ± 10.00 V amplitude at frequencies from 10^{-3} to 10^{5} Hz. Moreover, Ekiz *et al.* discussed a method for characterizing photovoltaic and photoconductivity effects on nanostructured surfaces through light-induced changes in XPS.[43] Their technique merges the chemical specificity of XPS with its sensitivity to the SPV, allowing the characterisation of photoconductivity under both static and dynamic optical excitation. They introduced a theoretical model that quantitatively describes the features of observed spectra, demonstrating its applicability on various sample systems, including solar cells and semiconductor nanoparticles. This approach underscores the potential of XPS to differentiate between surface voltage shifts due to photovoltaic or photoconductive effects, offering a pathway to predict the dynamic behavior under modulated illumination.

XPS-based SPV analysis offers an advantage over traditional Kelvin probe techniques by delivering extra chemical insights, which make it a valuable tool for semiconductor research.[44,45] A study by Oropeza *et al.*[44] examines the effect of surface photoreduction on the PEC properties of $CuBi_2O_4$, using XPS to study the surface reduction and its effect on the surface energetics and SPV. They report that irradiation of $CuBi_2O_4$ with photons ($h\nu \geq 2.7$ eV) in an inert atmosphere leads to the formation of reduced Cu on the surface. This reduction induces a downward band bending of 0.35 eV, enhancing the charge carrier transport properties, as evidenced by an increase in the characteristic SPV from 0.07 to 0.27 V. This remarkable finding constitutes the first experimental evidence of the beneficial effects of surface photoreduction on the PEC properties of $CuBi_2O_4$. Similarly, in their investigation of the InP interphase energetic optimization, Gao *et al.*[45] employed XPS in core and valence band regions to monitor the modulation of the surface energetics caused by the introduction of a buried p–n^+ junction, which favourably shifts the valence band edge to promote minority charge carrier's diffusion. They confirmed the enhancement of the charge carrier's diffusion length by XPS-based SPV measurements, using the binding energy shift of the P 2p and In 3d peaks upon *in situ* illumination, see Fig. 2a. They observed an increase in the SPV from 0.1 V to 0.35 V, and confirmed that the SPV of the n^+/p-InP depends on the light intensity with the relationship:

$$\mathrm{SPV} = \frac{kT}{e}\ln(1 - bI_0) \quad (2)$$

where I_0 is the incident light flux, b is a characteristic parameter of the semiconductor, which is constant under moderate band bending (BB >> kT) and e is the elementary charge. Eqn (2) predicts that SPV varies linearly with $\log(I_0)$ under moderate illumination, which was confirmed for their n^+/p-InP samples and should be taken as a general check measurement in the studies of SPV.

XPS of photoelectrodes under *in situ* illumination in NAP conditions. The introduction of near-ambient pressure XPS has allowed the study of adsorption processes of water, CO_2 and other reactant gases on the surface of photoelectrodes, providing key insights into the dissociation mechanisms which are key to understanding the overall artificial photosynthesis process. Although most of the NAP XPS studies have been carried out under dark conditions, important aspects on the catalytic performance of the photoelectrochemical processes have been addressed. Research has been focused on two major topics: (i) molecular dissociation (water or CO_2) process on semiconductor photoabsorbers or the co-catalyst/semiconductor interface, and (ii) effect of probe molecules on the chemistry and electronic structure of semiconductor photoabsorbers.

Zhang and Ptasinska conducted a series of studies of the water dissociation on model Ga-based photoelectrodes exposing GaP(111) and GaN(0001) to water vapour up to 5 mbar and temperatures from 298 to 773 K.[47–49] They found enhanced surface hydroxylation and oxidation of gallium on GaP[48] as the water pressure increased, with significant changes at temperatures above 673 K, leading to the formation of non-

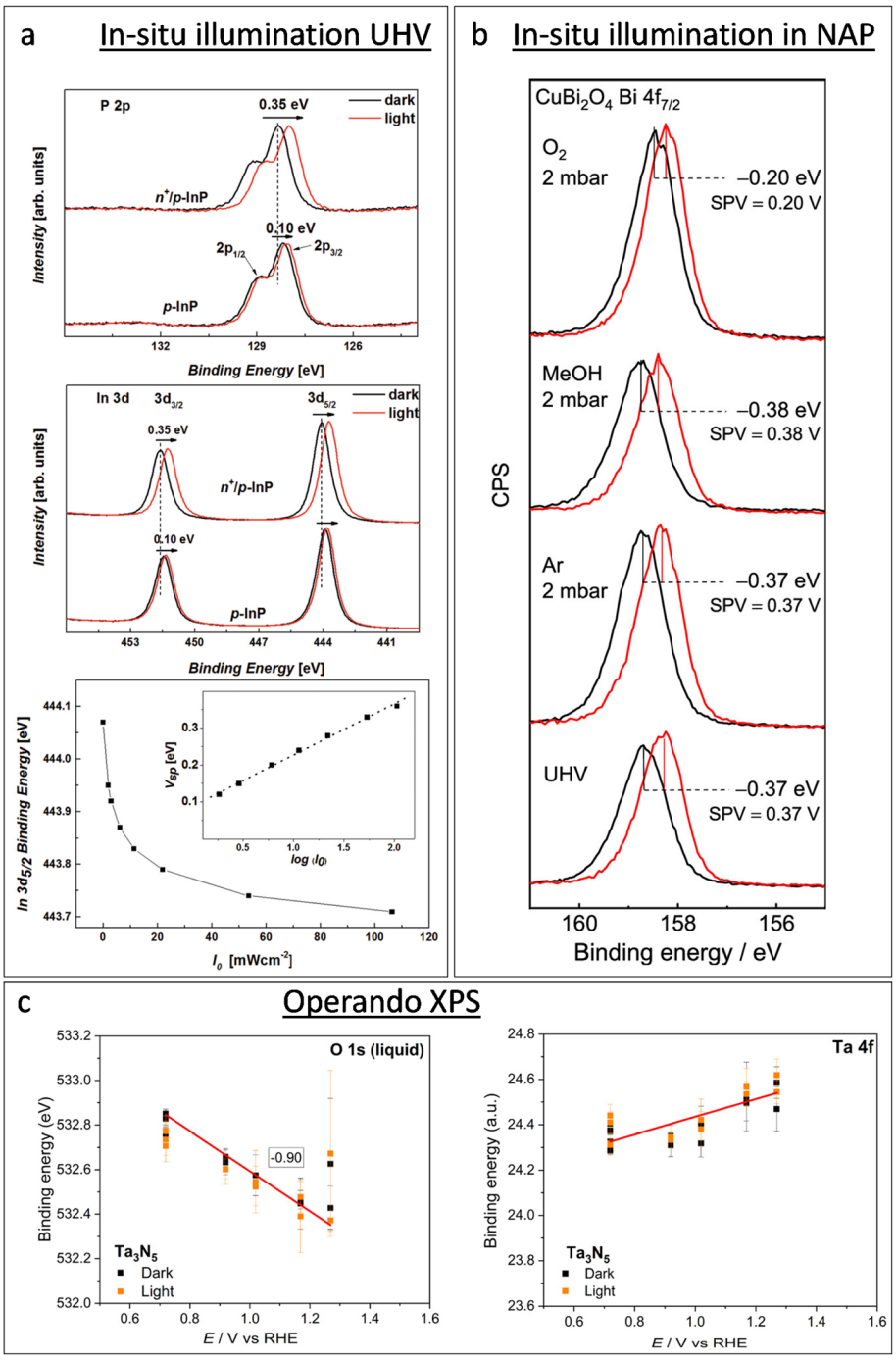

Fig. 2 Progress of *in situ* XPS studies from illumination in UHV *operando* XPS. (a) From top to bottom: XPS in the P 2p and In 3d regions of p-InP and n^+/p-InP in the darkness (black solid lines) and under illumination with an LED $h\nu^2 = 1.98$ eV (red solid lines), and In $3d_{5/2}$ binding energy shift for n^+/p-InP as a function of the incident light flux (I_0). The inset shows the surface photovoltage (SPV) as a function of log(I_0). Copyright 2016. Reproduced with permission from Wiley. Adapted from ref. 45. (b) XPS of a $CuBi_2O_4$ photoelectrode in the Bi $4f_{7/2}$ region, showing the XPS-based SPV measurement (spectra in black lines were recorded in the darkness, and spectra in red lines were recorded under light with a 405 nm laser) in UHV and in the presence of Ar, methanol vapour, and oxygen. Copyright 2019. Reproduced with permission from the American Chemical Society. Adapted from ref. 44. (c) Binding energy of the Ta $4f_{7/2}$ component and liquid contribution in the O 1s spectra during *operando* AP-XPS measurements for the Ta_3N_5 photoelectrode. Copyright 2023. Reproduced with permission from the American Chemical Society. Adapted from ref. 46.

stoichiometric gallium hydroxide and oxidation of phosphorus atoms. For GaN(0001), water dissociation at room temperature led to the formation of hydroxyl groups and a decrease in intrinsic upward band bending, enhancing its photocathodic properties. However, increased temperatures strengthened the chemical interaction, forming more oxides and hydroxides, which increased upward band bending and negatively affected GaN's photocathodic properties.[49] Additionally, their studies on

Pt/GaN(0001) revealed that water dissociates readily at the Pt/GaN interface, unlike on pure Pt surfaces.[47] This interface showed significant upward band bending, promoting the accumulation of photogenerated holes and enhancing oxidative dissociative adsorption of water, leading to the formation of hydroxyl groups and surface oxides bound to Pt, which are active catalytic sites for the hydrogen evolution reaction (HER).[50,51] Jackman *et al.* studied water adsorption on anatase TiO_2(101) using NAP-XPS,[52] finding that water adsorbs in a mixed molecular and dissociated state on stoichiometric surfaces. Sputtered surfaces exhibited similar characteristics, indicating that subsurface vacancies do not alter water interaction. The significant amount of adsorbed molecular water on TiO_2 suggests limited chemical interaction compared to more reactive surfaces such as GaP, InP, and GaN, where a more dissociative process occurs.[47–49]

The chemical and electronic interactions between photoelectrodes and adsorbates have also been an important topic of research using NAP-XPS. An early study by Salmeron *et al.* showed that the adsorption of O_2 (with a O_2 pressure of 1 torr) on the TiO_2 surface leads to a shift in the Ti 2p and O 1s core level binding energies towards a lower binding energy (by 0.4 eV), suggesting that the adsorption process involves the transfer of electrons from TiO_2 to O_2, resulting in such an upward band bending.[53] Mansfeldova *et al.* studied more specifically the effect of the environment on the surface work function (WF) of the TiO_2 photoelectrode.[54] Their NAP-XPS data showed a significant decrease in the surface WF of TiO_2 (by about 1 eV) upon water vapour exposure at 0.5 mbar, indicating a strong upward shift of the conduction band, which correlates with its photoanode behaviour in liquid electrolytes. The effect of the environment on the SPV of photoelectrodes is also accessible by NAP-XPS. Using *in situ* illumination under NAP-XPS conditions, Oropeza *et al.*[44] studied the effect of key electron donors and acceptors in the SPV of $CuBi_2O_4$ photocathodes, finding that while electron acceptors such as O_2 cause a reduction in the SPV, electron donors such as methanol cause an increase in the SPV (see Fig. 2b). Since XPS can simultaneously monitor the surface chemistry of the sample, the authors could correlate the diminution of the SPV with the re-oxidation of reduced Cu surface states, which led to the conclusion that those reduced Cu surface states are key achieving good photoelectrochemical properties of $CuBi_2O_4$.

XPS of photoelectrodes under *operando* conditions. Research on *operando* XPS of photoelectrodes has been particularly important in the context of artificial photosynthesis because it has been critical for understanding the dynamic chemistry occurring at the surface/interface of photoelectrodes during the PEC processes such water splitting and CO_2 reduction. Recent work has been focused on two main topics: (i) studies of the energetics at the photoelectrode/electrolyte interface and (ii) the generation of reaction intermediates at the surface of the photoelectrodes.

For instance, the research conducted by Lichterman *et al.*[55] provides a fundamental perspective on the operational characteristics of semiconductor/liquid junctions, in more realistic conditions than previous gas-phase-based NAP-XPS studies. Using the above-described dip-and-pull technique, they demonstrated how *operando* ambient-pressure XPS can be used to directly characterize the energetics of semiconductor/liquid junctions, focusing on the dynamics of semiconductor accumulation, depletion, and Fermi level pinning by defect states. In their work, the observed shifts in binding energy with respect to the applied potential directly revealed the ohmic junction nature at the liquid interface on metallized samples, and the rectifying junction behaviour at the liquid interface with semiconductor photoabsorbers. Furthermore, their findings on the behavior of metallized semiconductor/film contacts under varying conditions contribute to clarifying the mechanisms of charge transfers in photoelectrochemical cells. They highlighted that all parameters that can be directly observed by *operando* XPS are crucial variables for the design and operation of semiconductor–liquid junction devices for the PEC water splitting and CO_2 reduction. In a similar dip-and-pull approach, and introducing *in situ* illumination, Dahl *et al.*,[46] demonstrated that the semiconductor/electrolyte interfacial energetics of a tantalum nitride (Ta_3N_5) film, with and without a nickel oxide (NiO_x) protective layer, was explored under an applied bias under both dark and illumination conditions. Fig. 2c shows the variation in the binding energy of Ta 4f from the sample and O 1s from the electrolyte as a function of the applied potential under dark and illumination conditions. As expected, the O 1s peak position of the electrolyte shifts constantly with the applied potential; however, the Ta 4f peak position is independent of the applied potential under both dark and illumination conditions. The authors interpreted it as a direct evidence of Fermi-level pinning in Ta_3N_5 at the Ta_3N_5/electrolyte that effectively prevents band bending toward the Ta_3N_5/electrolyte. This means that there is no potential drop in the SCR that can promote the separation of photogenerated holes and electrons, which leads to poor PEC performance of bare Ta_3N_5. However, this work highlighted that surface passivation through the NiO_x layer could significantly reduce the recombination of photogenerated carriers, leading to increased surface band bending of Ta_3N_5, and better PEC performances. They did not find any clear oxidation of the Ta_3N_5, which correlated with the significantly larger photocurrents and stability of the NiO_x-coated materials. These types of *operando* XPS studies of the interface energetics provide key elements for the development of efficient and durable systems for water photoelectrolysis.

However, Favaro *et al.*[56] focused on bismuth vanadate ($BiVO_4$) electrodes in contact with an aqueous potassium phosphate (KPi) solution at an open circuit potential under both dark and light conditions, observing that visible light illumination triggers the formation of bismuth phosphate on the surface of the $BiVO_4$ photoanode. They suggested that this chemical modification leads to surface passivation that impacts the distribution of ions within the thin electrolyte layer due to the repulsive interaction between the negatively charged surface under illumination and the phosphate ions in the solution, which is observed as an increase in their photoelectron signals. Interestingly, they found that such light-induced changes at the $BiVO_4$/KPi electrolyte interface are fully reversible upon returning to dark conditions. Their findings emphasize the

significance of *in situ* methods to understand the impact of operational conditions on the performance of photoanodes.

These studies collectively illustrate the critical role of *operando* XPS techniques in advancing the field of photoelectrochemistry. By providing direct insights into the interfacial energetics and chemical states of photoelectrodes under operational conditions, researchers can better understand and mitigate the challenges of photoelectrode degradation and inefficiency. Such advancements not only contribute to the fundamental knowledge of photoelectrochemical mechanisms but also pave the way for the development of more robust and efficient solar fuel production systems. The current availability of several synchrotron stations capable of performing *operando* photoelectrochemical studies with robust setups is the optimal platform to establish routine analysis of photoelectrochemical systems and quickly advance on these ambitious scientific objectives. The possibility of adapting the new AP XPS instruments such as Polaris in DESY[57] and 3Sbar in ALBA (in construction phase), capable of performing XPS analysis at pressures of a few bars using tender X-ray sources, could provide more stable environments to establish routine analysis of photoelectrochemical systems. Moreover, in combination with the recently developed stroboscopic technique in MAX IV,[58] it could lead to the performance of time-resolved experiments in the microsecond range and allow the investigation of charge transfer dynamics and reaction mechanics in the microsecond time scale, exploiting this way the maximum potential of *operando* XPS experiments of photoelectrochemical systems.

In situ and *operando* X-ray absorption spectroscopy (XAS)

Synchrotron X-ray absorption spectroscopy (XAS) has been proven as a highly effective tool for material characterisation. Specifically, in XAS, the absorption of energy, carried by a photon, promotes an electron from a core-level to an empty orbital, monitoring the unoccupied electronic states, and hence, probing the local chemical environment (4–5 Å), providing information regarding the specific chemical bonds, oxidation states, spin states, site symmetry, and coordination environment.[59] In a typical XAS experiment, the monochromatic incident X-ray beam scans the vicinity of the absorption edge of an element, usually requiring a synchrotron X-ray source (with tuneable energy, high monochromatism and high intensity), even though there are currently available lab-scale XAS equipment.[60] Specifically, there are two ways of performing XAS experiments: (i) X-ray absorption spectra are recorded by measuring the ratio of the transmitted and incident X-ray beam intensities, known as the transmission mode, or (ii) the yield of secondary particles, fluorescence photons or emitted electrons, as a function of photon energy varying across the absorption edge of an element (total fluorescence yield, TFY, and total electron yield, TEY, respectively).[61] In transmission XAS, X-rays undergo attenuation while passing through the matter and intensity drops exponentially with the travelled distance, which is given as follows:

$$I_t = I_0 e^{-\mu x} \quad (3)$$

where I_t and I_0 are the transmitted and initial X-ray beam intensities, respectively, μ is the absorption coefficient and x is the thickness of the sample.[62] However, in TFY, also known as X-ray fluorescence (XRF), the emitted fluorescence X-rays after the interaction of the incident beam with the matter are measured as a function of the incident X-ray photon energy (E), and the absorption coefficient is given as follows:

$$\mu(E) \propto \frac{I_{fluo}}{I_0} \quad (4)$$

Finally, in analogy to XRF, the TEY measurements are based on the proportionality between the X-ray absorption coefficient and the emitted Auger electrons during the core decay as follows:

$$\mu(E) \propto \frac{I_{TEY}}{I_0} \quad (5)$$

Specifically, this experimental mode consists of measuring the total necessary applied current to compensate the photo-induced drain current in the sample.[63] Hence, every XAS spectrum represents the X-ray absorption coefficient, $\mu(E)$, of a system as a function of the incident X-ray photon energy. Besides, different regions can be distinguished in a typical XAS spectrum: (i) the pre-edge region, determined by the transition to the lowest unoccupied states, (ii) the X-ray absorption near-edge structure (XANES), also called near-edge X-ray absorption fine structure (NEXAFS), dominated by core transitions to quasi-bound states (multiple scattering resonances) for photoelectrons with kinetic energy in the range from 10 to 150 eV above the chemical potential and (iii) the extended X-ray absorption fine structure (EXAFS) region, associated with a weak scattering cross-section with neighbour atoms.

X-ray absorption spectroscopy (XAS) can be categorized into two measurement methods: hard-XAS, which employs high-energy X-rays to study bulk properties and heavy elements through core-level transitions, and soft-XAS, which utilizes lower-energy X-rays, offering surface sensitivity and probing valence band transitions for studying surface phenomena and organic material. Specifically, hard-XAS experiments are usually conducted in the transmission mode, which provides bulk-sensitive analysis and does not suffer from self-absorption effects.[59] However, due to the attenuation length of less than 1 μm, soft-XAS is usually measured through fluorescence and electron yield modes, having different probe depths.[64] The TFY technique shows an estimated probing depth of a few hundred nanometres, while TEY measurements are more surface-sensitive, with a probing depth of approximately a few nanometers.[65] Additionally, depending on the nature of the sample, different detection modes can work better. For example, sometimes, transmission XAS experiments can suffer from sample damage, caused by inhomogeneous concentrations or densities in the sample. To avoid this problem, transmission experiments require careful sample preparation and relatively concentrated samples, ideally in a light matrix. In contrast, the

fluorescence yield mode is more suitable for diluted samples or systems with heavy environments.[66]

In situ XAS measurements have been demonstrated to be essential for advancing our fundamental understanding of photoelectrocatalysis and accelerating the development of efficient catalytic materials for sustainable energy technologies. This spectroscopy allows monitoring changes in the chemical and electronic states of the catalyst in real time as they undergo photoelectrocatalytic reactions. This real-time monitoring provides information on reaction mechanisms, intermediate species, and reaction kinetics that are difficult to obtain using *ex situ* techniques. Besides, XANES and EXAFS can provide information about the local coordination environment and electronic structure of catalytic materials. This information helps in identifying the active sites responsible for catalytic activity, facilitating the design of more efficient catalysts.

In general, the experimental requirements for performing *in situ* and *operando* (hard)-XAS measurements are easier than those for XPS mainly due to the vacuum requirements, which make the development of *in situ* electrochemical cells much more complicated. Due to this reason, a considerable higher number of studies have reported *in situ* and *operando* (hard)-XAS measurements in electrodes for solar fuel generation compared to *in situ* and *operando* XPS.[67,68] However, still limited studies have reported *in situ* XAS on photoelectrodes, as X-ray absorption measurements with photoelectrochemical cells require complex engineering to ensure compatibility and functionality of both systems simultaneously, compared to the *in situ* study of electrocatalysts.[69,70] This involves designing specialized cells that can accommodate both X-ray transparency and photoelectrochemical functionality. Furthermore, most relevant chemical and electronic changes in photoelectrochemistry occur on the surface of the electrode, and not in the bulk, further complicating the collection of reliable data that provide true and reliable information. Thus, due to the bulk nature of the XAS technique compared with the shallow nature of the changes under PEC conditions in the photoelectrodes, there are mainly two ways to perform *in situ* experiments: (i) to fabricate really thin films of the photoelectrode under study, trying to maximize the surface-to-volume ratio or (ii) to investigate the induced changes in a co-catalyst by the effect of the photogenerated carriers in the absorbing material. Both types of studies are considered in the present review.

Among the characterisations of photoelectrodes for solar fuel generation by *in situ* and *operando* XAS, much effort has been devoted to study the oxidation reactions, mainly oxygen evolution reaction (OER), and hence, to characterise n-type semiconductors. However, there have already been some recent works that report *in situ* XAS in p-type photocathodes for the hydrogen evolution reaction (HER), and the challenging CO_2 reduction reaction (CO_2RR), as well as N_2 fixation (N_2RR) to ammonia (NH_3).

Regarding photocathode analysis, in 2020 Chen *et al.*[71] investigated bimetallic Ni-based p-Si micropillar photocathodes through *in situ* XAS for solar-driven HERs. The authors incorporated Ni/Mo, Ni/Co, and Ni/Fe into silicon electrodes and analysed the effect of incorporation of Mo, Co and Fe on the photoelectrochemical properties, finding out that the most active is the Ni/Mo combination (Fig. 3a). To investigate the oxidation state and local atomic environment under photoelectrochemical conditions, they performed *in situ* XANES measurements in the liquid medium. A custom reaction cell designed for this *in situ* measurement was used, but the authors do not provide details or schematics about its design. After introducing NiMo/p-Si MPAs in the alkaline electrolyte, no noticeable change was observed in the Ni K-edge spectra (Fig. 3b). However, under cathodic conditions, above 0 V, they found out that Ni XANES edge shifted to a higher energy, indicating an increase in the Ni valence state (Fig. 3c). Interestingly, when the same potential is applied to the NiCo/p-Si and NiFe/p-Si MPAs, negative changes in the absorption energy can be observed, indicating that the reduction of Ni was caused by the cathodic potential during the HER (Fig. 3d and e).

Furthermore, by *in situ* EXAFS, the authors analysed the local atomic environment. Once the HER starts, the peak intensity of the Ni–O scattering path at 1.4 Å in the NiMo/p-Si sample significantly increased. This effect is not observed in the rest of the electrodes. The scattering paths of Ni–Ni were mostly unchanged in all cases. Besides, the intensity of the Ni–O peak in NiCo/p-Si MPAs decreased, indicating that the nickel oxides were changed into the metallic state during the reaction. These *in situ*-formed Ni-species might be considered as the active intermediates for the high activity of NiMo/p-Si MPAs. Other researchers correlated the HER activity with the NiO introduction on the Ni surface before.[72] According to these results, the authors suggest that the growth of the high-valence Ni (hydr) oxides during HERs could favour the photoelectrochemical properties in alloy-based photocathodes.

Furthermore, Wang *et al.* investigated silicon-based photocathodes for photoelectrochemical (PEC) nitrogen reduction to ammonia, aiming to emulate the natural reaction processes, involving multiple protonation and electron transfer steps. They designed a two-cell electrochemical system to enhance the PEC nitrogen reduction reaction (NRR) efficiency. This system included a stainless-steel mesh cathode modified with encapsulated Fe_3C nanoparticles and amorphous carbon. The two cells, physically and electrically separated, allowed the N_2 feed gas to pass through the porous electrode of the first cell (C2) before reaching the working photocathode in the second cell (C1). In 2021, they reported significant improvements using this setup on a Au/SiO_2/Si photocathode, achieving an NH_3 yield rate of 22.0 μg cm^{-2} h^{-1} and a faradaic efficiency (FE) of 23.7% at −0.2 V *vs.* RHE. Without the stainless-steel-based cathode, the yield rate and FE were markedly lower, at 6.6 μg cm^{-2} h^{-1} and 7.2%, respectively.[73] First, XPS was used to track changes in the oxidation states of the Au/SiO_2/Si photocathode before and after illumination. The survey scans showed similar characteristic peaks for Au 4f, Si 2p, and O 1s under both conditions. High-resolution XPS spectra revealed a decrease in the Au^{1+}-to-Au^0 ratio under illumination, and a higher Si^{4+}-to-Si^0 ratio compared to dark conditions.

Additionally, *operando* XAS was used to explore the chemical environment under working conditions. The XANES spectra at the Au L_3 edge (Fig. 4a) indicated that the oxidation state of Au

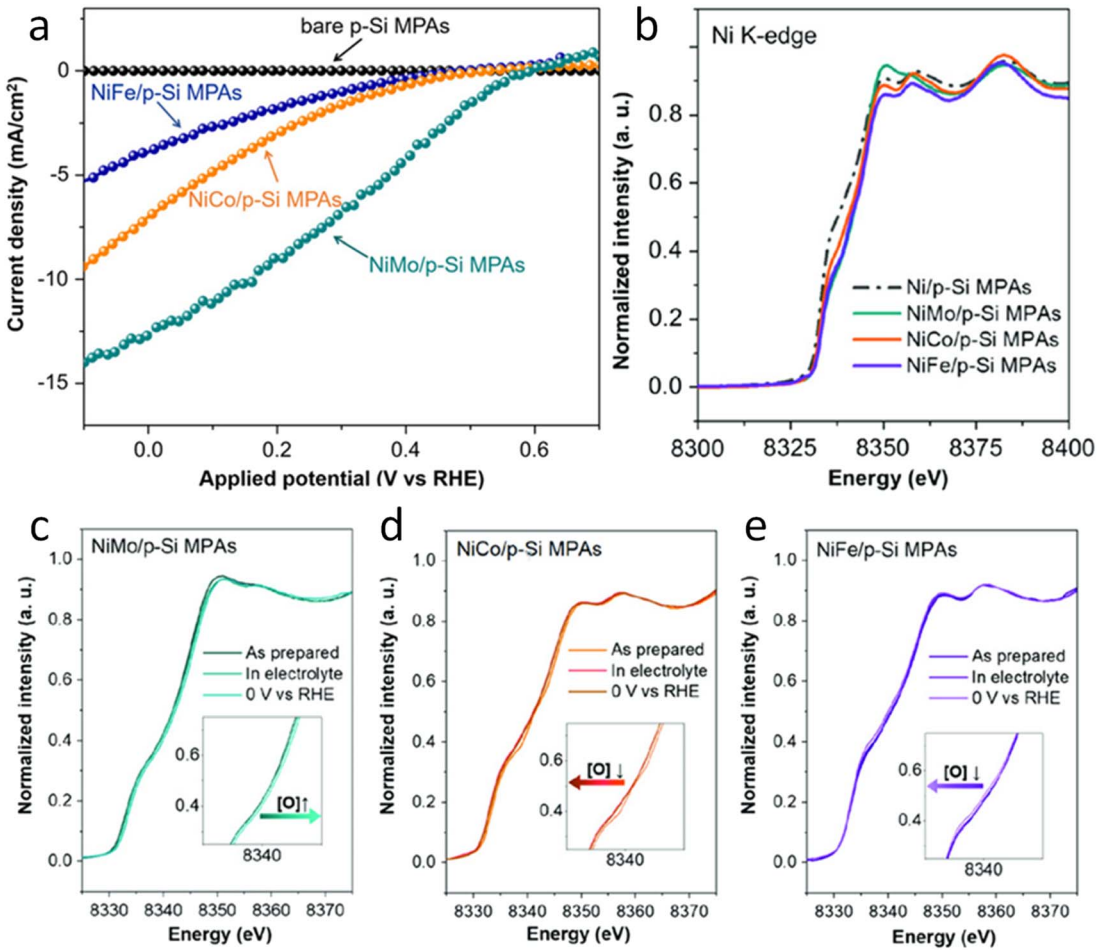

Fig. 3 (a) Photoelectrochemical characterisation of the Ni-based alloys/p-Si MPA photocathodes in 1 M KOH under illumination. (b) Normalized Ni K-edge XANES spectra of the p-Si MPAs/alloy photocathodes. (c–e) Ni K-edge of *in situ* X-ray absorption spectroscopy measurements of the Ni-based alloys/p-Si MPAs during the photoelectrochemical hydrogen production reaction. Copyright 2020. Reproduced with permission from Wiley. Adapted from ref. 71.

was related to the intensity of the white line (WL) peak at ~11 920 eV. The Au L_3 edge XANES difference spectra (Fig. 4b) revealed a WL peak at ~11 920 eV, which intensified with the increasing Au oxidation state.[74] This peak intensity varied with different photoelectrode potentials and the presence of the modified stainless-steel cathode, correlating with changes in the PEC NRR efficiency. The system with the modified stainless-steel cathode maintained at −0.2 V *vs.* RHE exhibited the highest oxidation state of Au, suggesting an increase in vacancies at the Au 5d valence level. Besides, Fourier transform k_3-

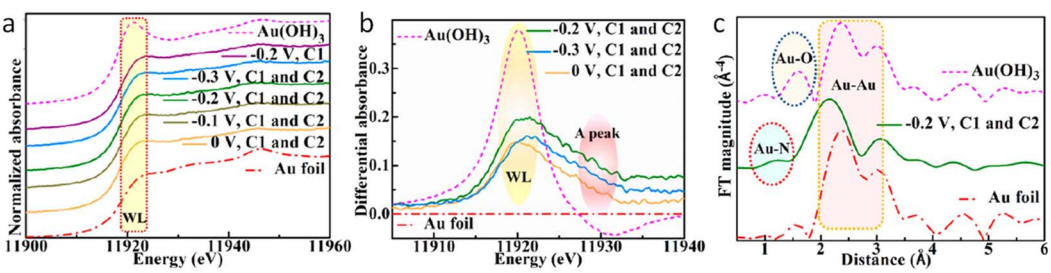

Fig. 4 *Operando* XAS of the Au/SiO_2/Si photocathode in the NRR PEC process. (a) Au L_3-edge XANES spectra with and without the excitation of a modified stainless-steel cathode at each given photoelectrode potential during the PEC NRR. (b) Comparison between the Au L_3-edge XANES difference spectra of the photocathodes with a modified stainless-steel cathode at different photoelectrode potentials. The Au foil as the baseline was chosen to obtain various difference spectra. (c) Fourier transform of the experimental EXAFS spectra of the photocathode with the modified stainless-steel cathode at −0.2 V *vs.* RHE, Au foil, and Au $(OH)_3$. Copyright 2021. Reproduced with permission from the American Chemical Society. Adapted from ref. 73.

weighted EXAFS spectra (Fig. 4c) under reaction conditions showed contributions from Au–Au bonds and a new peak at ~1.3 Å, attributed to Au–N coordination, which was not present in less efficient PEC NRR reactions. The single-cell system, lacking the modified stainless-steel cathode, showed a lower Au oxidation state and reduced HER performance. The study suggested that the modified stainless-steel cathode first activates N_2 molecules at the optimal potential, forming active nitrogen species that adsorb onto the surface of Au NPs, enhancing covalent bonding and improving the PEC NRR performance on the Au/SiO_2/Si photocathode.

In 2023, the same group investigated the role of the synergy between electron localization and alloying Au, Co and Pd (ACP) in determining the photoelectrochemical conversion of nitrogen to ammonia in the multilayered AuCoPd-CoO_x/SiO_2/Si photocathodes.[75] On the one hand, XPS analysis showed that while Au and Pd maintained their peak positions under illumination, their average oxidation levels decreased. The peak positions associated with Co were unaffected, but the Co^{x+}/Si^{4+}-to-Co^0/Si^0 ratio increased, differing from Au and Pd trends. These tests were pseudo *in situ* since no potential was applied. On the other hand, as in their previous work, the XANES spectra of the Au L_3 edge indicated that ACP samples had spectra similar to those of the Au foil and different from those of $Au(OH)_3$. The ACP sample performed better than the Au-only sample. At the highest yield potential (−0.3 V *vs.* RHE), the ACP sample showed the highest Au oxidation state, indicating maximum formation of hybridized chemical bonds during the PEC NRR. EXAFS spectra revealed consistent Au–Au bonds across all bias potentials. However, the intensity of the ~2.0 Å peak, corresponding to the Au–Pd bonds, increased as the applied potential decreased, peaking at −0.3 V *vs.* RHE. This increase reflected the enhanced formation of the AuPd alloy due to greater reduction of Ag^+/Pd sites under illumination.

In 2021, Sawangphruk *et al.* analysed a cobalt-based photocathode by *in situ* XAS.[76] Specifically, the authors investigated cobalt hydroxide nanosheets as photoelectrodes and the effect of silver particles on the optical properties and conductivity. This material is usually used as an electrode material for various energy storage and conversion applications,[77] and recently, it has been reported as a photoactive material.[78,79] Photon energy can cause cobalt hydroxides to generate charge carriers. This process can generate additional photocurrent, leading to higher performance when $Co(OH)_2$ is used as the electrode. However, their intrinsic electronic and electrical conductivities are very poor, and the introduction of AgNPs can be a solution to overcome these problems. In this work, the authors claim that under dark conditions, AgNP-doped α-$Co(OH)_2$ shows a higher capacitance than that of undoped β-$Co(OH)_2$, and the authors attributed this to its higher electrical conductivity and, therefore, faster charge transfer. However, under illumination, while an improvement in the charge storage performance of undoped $Co(OH)_2$ is observed, the opposite phenomenon occurs with the addition of Ag. The excessively narrow band gap and the competitive surface of the resonance process of the plasmon occur in parallel on the AgNP surfaces, leading to less charge capacity performance. In this sense, the change in the oxidation state of Co during the electrochemical process is crucial evidence to investigate the charging mechanism of electrode materials. To gain a deep understanding of the local structural change in Co and its pseudocapacitive behavior when the photoelectrodes are charged and discharged, the authors carried out *in situ* XAS experiments by analyzing the XANES spectra of the Co K-edge. To do that, the authors used an electrochemical cell developed for a previous work.[80] Then, they analysed the Co K-edge XANES spectra of α-$Co(OH)_2$ Ag doped with the AgNP photoactive electrode under light and dark conditions at different potentials. The average oxidation state of Co in Ag–$Co(OH)_2$ is +2.58 at an energy edge of 7719.89 eV. This result refers to mixed valences of Co^{2+}/Co^{3+}. The initial oxidation state of Co in α-$Co(OH)_2$ Ag doped in 1 M NaOH was found to be +2.46 eV. Under −0.4 to 0.1 V *versus* SCE bias potential, the edge positions change significantly to a higher energy for both conditions, indicating an increasing oxidation state of Co during the charging process. Under dark conditions with the fully charged state of Ag-doped α-$Co(OH)_2$, the oxidation state of Co increases to +3.08, while under light illumination it was +3.14. The higher oxidation number of the Ag–$Co(OH)_2$ electrode under illumination was attributed to the photovoltaic effect, which generates the photoelectrons. However, the oxidation state of Co in Ag–$Co(OH)_2$ under dark conditions is +3.0, while under light irradiation, it decreases to +2.92. The conclusion they reached was that when the Ag-doped α-$Co(OH)_2$ photoelectrode is discharged, the photoelectrons can recombine with the holes generated in the CB, while the photoexcited electrons under dark conditions were transferred to the external system.

In the case of photoanode materials, hematite, Fe_2O_3, and bismuth vanadate, $BiVO_4$, stand out as the most studied candidates for PEC oxidation reactions and are the most studied semiconductors with *in situ* and *operando* synchrotron XAS. Specifically, hematite (α-Fe_2O_3) photoanodes have attracted increasing attention as photoanode materials for photoelectrochemical applications thanks to their adequate bandgap, abundance and stability.[81] Although progress has been made to achieve highly efficient hematite photoelectrodes for the OER,[82] understanding the nature of recombination and charge transfer processes using X-ray-based techniques is essential.[83] In this sense, XAS measurements have been used to correlate the presence of defects in hematite photoanodes with changes in their photoelectrochemical behaviour. *Ex situ* FT-EXAFS of the Fe K-edge revealed that the peak intensity corresponds to whether the Fe–O or Fe–Fe bonds can be reduced when oxygen vacancies are present.[84] Mesa *et al.*, have recently reported *in situ* XAS showing that the Fe–Fe bond signal, in the Fe K-edge FT-EXAFS data, reduces when applying a positive potential (1.5 V *vs.* RHE compared to open circuit potential conditions) in oxygen vacancy-containing hematite photoelectrodes (Fig. 5a).[85] The application of an oxidative potential resulted in a slight shift of the absorption edge in the XANES measurement towards positive energies, which was tentatively associated with the Fe^{2+}/Fe^{3+} oxidation, given that the presence of oxygen vacancies in the hematite structure would generate Fe^{2+} atoms. Similarly, for M-doped α-Fe_2O_3 photoanodes (where M = Nb or

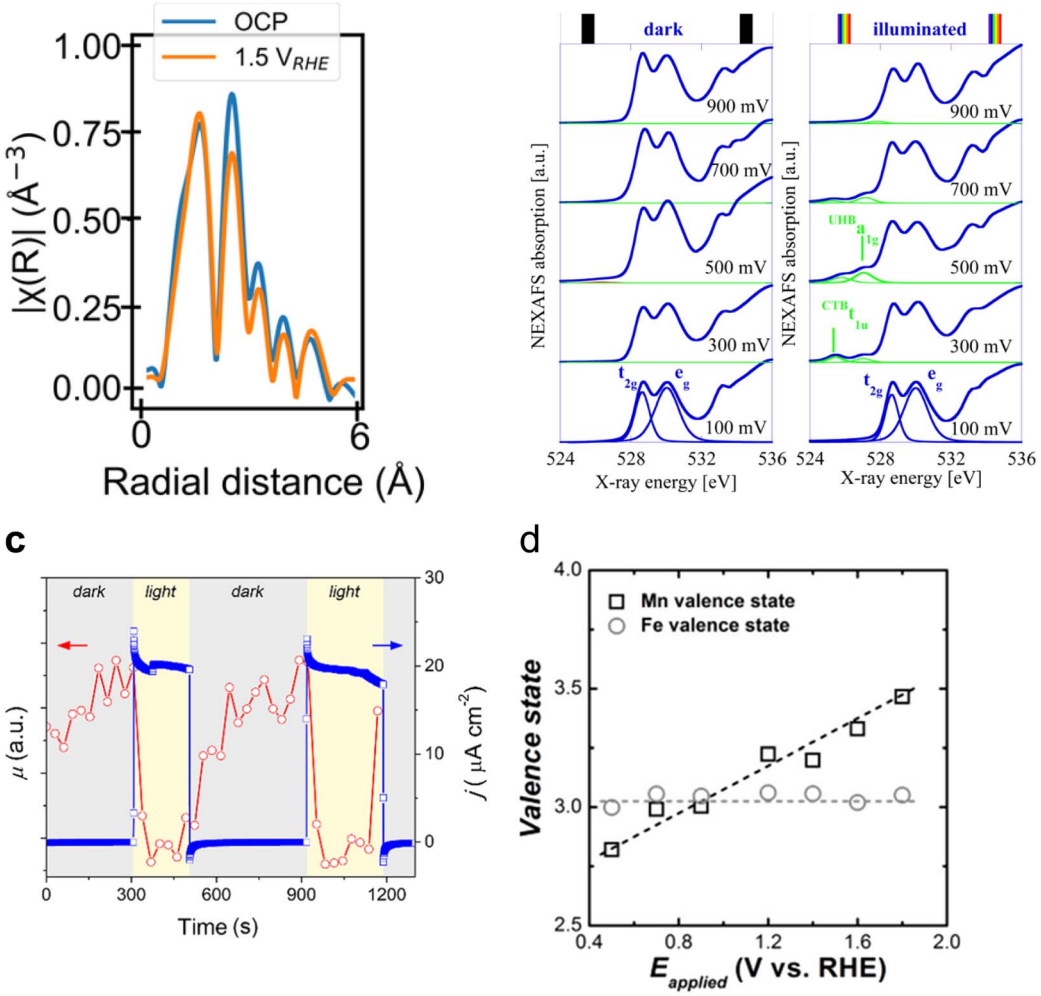

Fig. 5 (a) R-space plot of the Fe K-edge XANES spectra of the hematite (α-Fe_2O_3) photoanode in the open circuit potential (*i.e.*, no applied potential, blue trace), applying 1.5 V *vs.* RHE (orange trace). Copyright 2024. Reproduced with permission from Springer Nature. Adapted from ref. 85. (b) O 1s NEXAFS spectra recorded at bias from 100 to 900 mV under dark (left) and light (right) conditions. Copyright 2012. Reproduced with permission from the American Chemical Society. Adapted from ref. 86. (c) X-ray absorption coefficient (μ) at a fixed energy of 8350 eV and photocurrent density at a fixed potential of 1.3 V acquired simultaneously, switching the light on and off. Copyright 2020. Reproduced with permission from the American Chemical Society. Adapted from ref. 87. (d) Valence states of Mn and Fe on α-Fe_2O_3/$Mn_3O_{4+\delta}$ photoanodes during the photoelectrochemical OER. Copyright 2018. Reproduced with permission from the American Chemical Society. Adapted from ref. 88.

Ta), an increased X-ray absorption of the Fe L-edge, upon illumination, was observed for the doped hematite photoelectrodes.[89] This increased absorption was assigned to enhanced electron transfer in the Fe 3d conduction band of hematite, giving rise to the observed improved photocurrent.

However, both O 1s NEXAFS and O K-edge measurements have been used to investigate the electronic structure of the photogenerated electrons and holes in hematite photoanodes.[90] For example, *ex situ* time-resolved O K-edge XAS was used to identify the transient (~0.3 ps) formation of O 2p hole states upon photoexcitation.[91] Interestingly, Braun *et al.* identified two transitions in the pre-edge region of the *in situ* O 1s NEXAFS as a function of applied potential under light and dark conditions. These two transitions appear to be separated by 1.5 eV and were assigned to photogenerated holes of both Fe 3d and O 2p character (Fig. 5b).[86] Although changes in the O 1s NEXAFS due to changes in the filling state of oxygen vacancies have not been ruled out,[92] evidence of the electronic and chemical nature of photogenerated holes, in particular those at the surface, is still lacking.

Interfacing photoelectrodes with electrocatalysts to enhance charge transfer to the electrolyte is a highly used engineering strategy in PEC applications. Thus, studying and understanding the interface is crucial for producing highly efficient photoelectrode architectures. For example, Naldoni *et al.* studied the charge transfer at the interface between hematite and a highly active OER electrocatalyst, NiO_x, by means of fixed-energy XAS under both potentiostatic and galvanostatic conditions.[87] In this work, the authors probed the Ni K-edge to probe the hole transfer from the hematite photoanode to the NiO_x catalyst layer prior to the OER. Interestingly, under photoelectrochemical water oxidation conditions, the differential XANES spectra (light–dark) coincided with the differential XANES spectra of γ-NiOOH–$Ni(OH)_2$ standards. Given that, in

NiO_x electrocatalysts, the active species towards the OER are reported to be NiOOH. Naldoni *et al.* assigned their differential XANES spectra to the accumulated OER active species formed after a hole transfer process from hematite. Additionally, the authors performed time-resolved (in the s timescale) X-ray absorption of a fixed energy (8350 eV), thus probing the X-ray absorption coefficient of NiO_x during the OER (Fig. 5c). The observed reduction in the X-ray absorption coefficient, measured at 1.3 V, was assigned to the transformation of $Ni(OH)_2$ into NiOOH, which is recovered upon turning off the light.[87] A similar system, but with a NiFeOOH electrocatalyst, was studied by Ismail *et al.*, reporting, through a linear combination analysis, that a γ-FeOOH phase is formed at the α-Fe_2O_3/NiFeOOH interface under illumination at a positive potential (Fig. 6).[93]

The increase in the PEC water oxidation rate upon the deposition of co-catalysts, based on metals such as Co and Mn, on α-Fe_2O_3 photoanodes has also been investigated by *in situ* XAS means. For example, Lange *et al.* measured the Co K-edge on α-Fe_2O_3/CoB_i (cobalt borate) photoanodes *in situ*.[94] In this work, the authors, through the use of Co standards with precise oxidation states, calculated a slightly higher Co oxidation state when photodeposited on hematite than when grown on FTO. This was assigned to a built-in potential at the α-Fe_2O_3/CoB_i interface. Additionally, *in situ* measurements revealed that CoB_i oxidises by accepting holes from hematite, and the authors suggest that a fraction of them oxidise water. Similarly, Liu *et al.*, reported an increase in the oxidation state of Mn in α-Fe_2O_3/$Mn_3O_{4+\delta}$ photoanodes during the photoelectrochemical OER.[88] However, in this case, the authors did not observe any change in the oxidation state of Fe and suggested the transfer of holes from hematite to the $Mn_3O_{4+\delta}$ catalyst (Fig. 5d). It is possible that the authors did not observe any changes in the absorption of the Fe K-edge, given the thickness of the reported photoelectrode.

In general, it is apparent from the reported studies that the oxidation of the metal centers in co-catalyst overlayers can be readily monitored by *in situ* XAS, most probably due to the low thickness exhibited by such co-catalyst's layers. Once the holes transfer to thin layers of co-catalysts, metal centers oxidise and a change in the X-ray absorption edge is more straightforward to observe and quantify. As such, to further determine the nature of photogenerated holes, in bare hematite photoelectrodes, which are active for the OER, it is key to use thin α-Fe_2O_3 photoanodes.

Moving to $BiVO_4$, Lifei Xi *et al.*[95] reported the study of a MnPi catalyst layer over a $BiVO_4$ photoanode by *in situ* soft X-ray absorption spectroscopy (XAS) at the Mn L-edge upon varying the applied potentials and the illumination conditions (Fig. 7). As explained before, *in situ* NAP-XPS is the most suitable approach for PEC conditions, but it can be challenging to obtain reproducible spectra due to the varying thickness of the electrolyte layer and possible pressure changes inside the experimental chamber.[33] Because of that, the authors of this work focused on soft-XAS, because while hard-XAS probes the transition metal K-edge, with soft XAS, the metal L-edge is probed, which is more favourable for deciphering mixtures of oxidation states due to the narrower natural line widths (Mn K-edge, 1.12 eV; Mn L-edge, 0.32 eV).[96] To conduct these experiments, the authors developed an *in situ* and *operando* cell.[97,98] In these works, the authors reported an innovative design for an *operando* soft X-ray transmission and fluorescence cell that allows rapid membrane replacement and simpler operation compared to earlier designs. Specifically, the cell consists of three chambers (a vacuum chamber and two helium-filled chambers) separated by silicon nitride (Si_3N_4) membranes. This cell allows for the confinement of a liquid or electrolyte between these membranes and supports the application of both electrochemical techniques and visible light. It includes a gold-coated membrane for conductivity, photodiodes for detecting transmission and fluorescence signals, and LEDs for visible light application. The helium pressure can be regulated to adjust the liquid layer thickness, and the cell can be precisely positioned using a translational and angular stage, facilitating *in situ* studies of solid/liquid interfaces with X-ray absorption spectroscopy. Specifically, Mn L-edge spectra under different applied potentials and light conditions were studied. The authors found that the photogenerated holes transferred into the MnPi layer and to the electrolyte interface were enhanced by band bending in the semiconductor under illumination, which is related to an increased potential by a built-in photopotential. They also found that the photogenerated holes could oxidize the MnPi co-catalyst layer even under open circuit potential conditions. Then, when increasing the applied bias, the

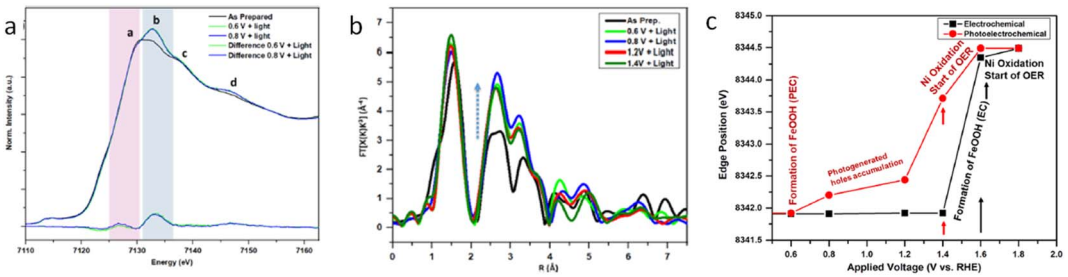

Fig. 6 *Operando* XAS of iron in the α-Fe_2O_3/$Ni_{0.8}Fe_{0.2}OOH$ photoanode. (a) Iron K-edge XANES at different applied potentials under illumination. (b) FT-EXAFS of Fe at different applied potentials under illumination. (c) Plot of the α-Fe_2O_3/$Ni_{0.8}Fe_{0.2}OOH$ photoanode at different applied potentials in the darkness (EC) and under illumination (PEC), explaining the OER mechanism. Copyright 2021. Reproduced with permission from the American Chemical Society. Adapted from ref. 93.

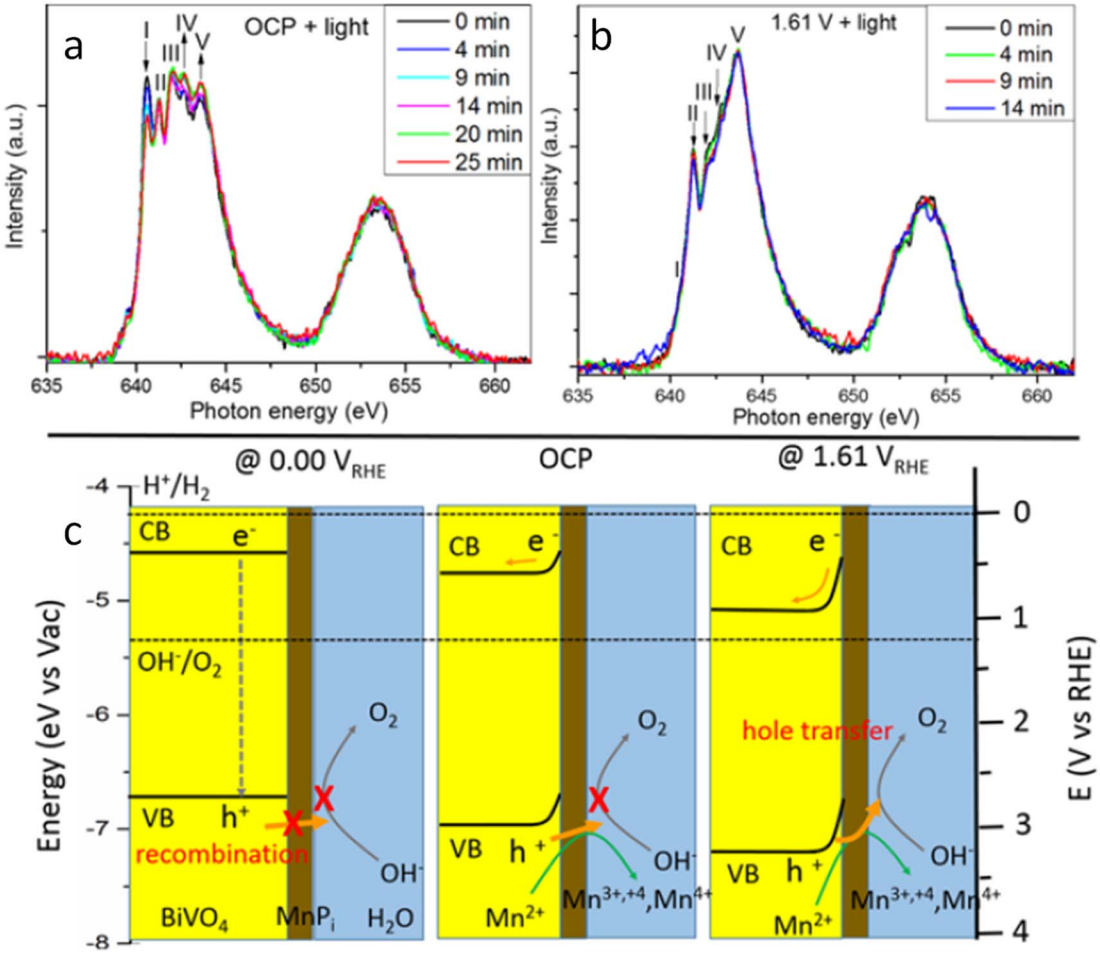

Fig. 7 Temporal evolution of XAS spectra of a MnPi-modified $BiVO_4$/Au/Si_3N_4 photoanode in a 0.1 M KPi buffer solution with KNO_3 added at (a) OCP and (b) 1.61 V under light. (c) Schematic illustration of the photogenerated carrier transfer from the $BiVO_4$ photoanode to the MnPi film at 0.00 V, OCP condition, and 1.61 V *vs.* RHE. Copyright 2017. Reproduced with permission from the American Chemical Society. Adapted from ref. 95.

electronic and crystalline structures of the MnO_x layer were changing to a birnessite-type layer structure associated with the electron migration from the MnPi film into the $BiVO_4$ photoanode. The formation of birnessite must be accompanied by the incorporation of K^+ between the MnO_6 layers, leading, for example, to a KMn_8O_{16} phase. These experiments were able to conclude that Mn^{3+} species, instead of Mn^{4+}, in birnessite were the active sites for the OER.

A couple of years later, some of the team members of a previous work, Lifei Xi and coworkers,[99] studied a NiBi co-catalyst over a $BiVO_4$ photoanode by *in situ* soft and hard XAS. The authors successfully unravel the electronic structure of NiBi-modified $BiVO_4$ photoanodes under working conditions (Fig. 8a) and understand the OER catalytic cycle and the formation of active sites (Fig. 8b). The authors showed that Ni was in +2 state in the electrodeposited amorphous NiBi film and it was readily oxidized up to +4 state under OER conditions. This work reported, for the first time, the direct observation of Ni^{4+} species during light-driven water oxidation. They also observed that the oxidation of Ni was accompanied by an O K-edge prepeak at 529.17 eV. Specifically, the formation of Ni^{4+} was associated with the formation of electron-deficient oxygen sites. These sites acted as electrophilic centers leading to the formation of a stable precursor state prior to O–O bond formation. Finally, cyclic voltammetry-XAS results supported that the formation of Ni^{4+} occurred before the formation of partly electron-deficient oxygen sites.

All the above-explained works have demonstrated how *in situ* XAS measurements are a powerful tool to determine the catalytic mechanisms (even catalytic cycles) in photoelectrodes, achieving a true understanding of these materials under relevant working conditions. It is also crucial to develop a correct design for the photoelectrochemical cells, which allows the performance of the *in situ* and *operando* experiments with all the above-mentioned requirements. In general, the photoelectrochemical cells found in the reported studies are custom-made, either 3D printed or machined to work in both fluorescence and transmission modes. Fig. 9 displays different PEC cell designs and configurations. First, two examples for *in situ* XAS measurements in fluorescence mode are shown in Fig. 9a

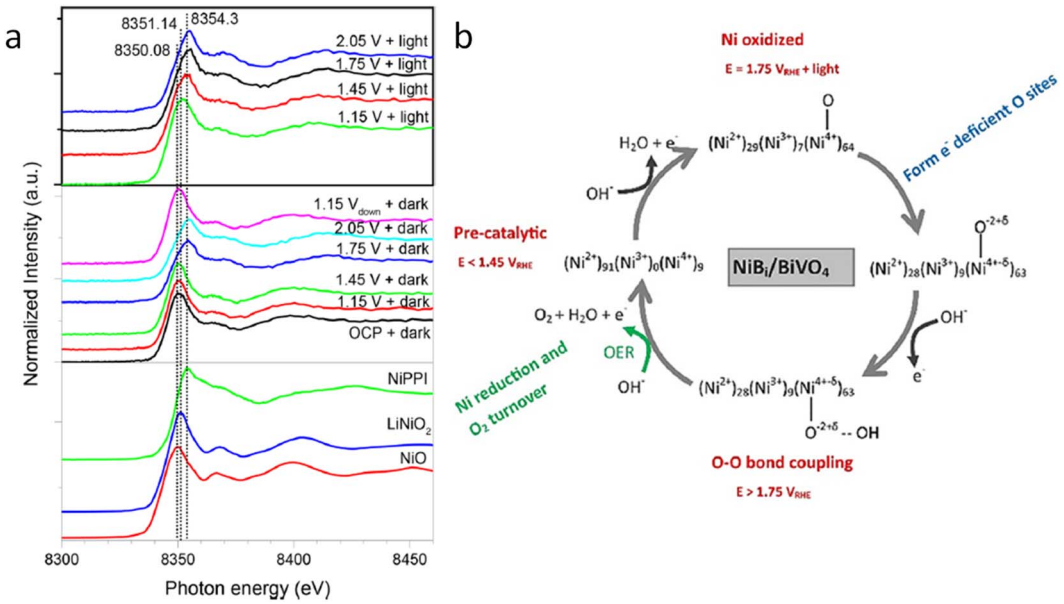

Fig. 8 (a) *In situ* Ni K-edge spectra of the NiBi/$BiVO_4$ photoanode at different potentials under illumination. (b) Schematic showing the NiBi co-catalyst change observed *in situ* XAS measurements of the NiBi/$BiVO_4$ photoanode. Copyright 2019. Reproduced with permission from the American Chemical Society. Adapted from ref. 99.

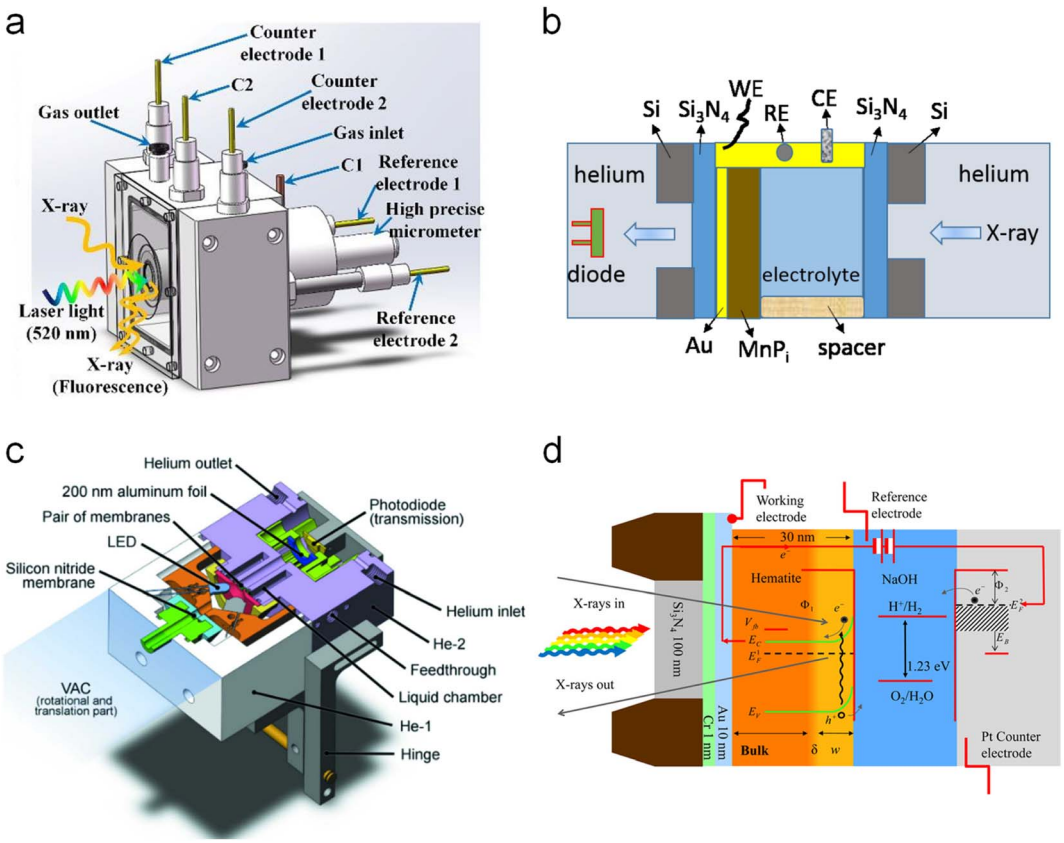

Fig. 9 Different cell configurations for *in situ*/*operando* XAS experiments. (a) Copyright 2021. Reproduced with permission from the American Chemical Society. Adapted from ref. 73. (b) Copyright 2017. Reproduced with permission from the American Chemical Society. Adapted from ref. 97. (c) Copyright 2016. Reproduced with permission of IUCr. Adapted from ref. 98. (d) Copyright 2012. Reproduced with permission from the American Chemical Society. Adapted from ref. 86.

and b. Fig. 9a shows a (photo)electrochemical cell with an X-ray and visible light transparent window, *i.e.*, Mylar, and the sample illumination is from the photoelectrode/electrolyte interface. In this type of photoelectrochemical cell, the thickness of the electrolyte that the X-rays have to travel through is between 0.1 and 1 mm and the sample is illuminated from the same direction of the X-ray irradiation, both to the front of the sample.[73,100,101] Similarly, Fig. 9b shows a cell configuration where the photoelectrode is directly prepared on a X-ray transparent material such as Si_3N_4, thus X-ray irradiation and fluorescence are performed through the back of the photoelectrode. In this case, the electrolyte thickness plays a less relevant role and the illumination is achieved from the front of the photoelectrode.[86,102] Alternatively, when the photoelectrode is deposited on a non-X-ray transparent material, such as FTO, the photoelectrode can be placed facing the X-ray transparent window, where Kapton, Si_3N_4 and Mylar have been used at maximum 1 mm distance. In this configuration, the X-ray irradiation comes from the front (*i.e.*, electrode/electrolyte interface) and the visible excitation is performed through a mica/quartz window at the back of the photoelectrode.[87,93] On the other hand, for measurements of soft X-rays, XAS in transmission mode is presented in Fig. 9c and d. Fig. 9c shows the schematic illustration of a tight (photo)electrochemical cell able to support measurements under vacuum by having integrated the illumination system, by LEDs, in the electrochemical chamber.[98] Similarly, Fig. 9d presents a cell configuration where the catalyst can be deposited on an X-ray-transparent, Au-coated Si_3N_4 membrane.

In situ and *operando* X-ray diffraction (XRD) and X-ray scattering (XRS)

Diffraction happens with the scattering of incident X-rays by a certain material at different angles. Scattered X-rays are intense in some directions, as a result of constructive interferences, and deficient in other ones, due to destructive interferences. The constructive interference can be explained by Bragg's law, given as follows:

$$2d_{hkl}\sin(\theta) = n\lambda \quad (6)$$

where *hkl* are the Miller indices for identifying the crystallographic planes, d_{hkl} represents the distance between parallel planes, which is a function of the unit cell characteristics (shape and size), θ is half of the angle between the incident and scattered beams, n is an integer corresponding to the plane from which the beam is scattered, and λ is the wavelength of the incident light.[103] An XRD spectrum represents the X-fay diffraction intensity at different scattering angles, where the structure and size of the analysed material produce a certain XRD pattern. During the past few decades, different diffraction-based techniques have been developed for different applications.

X-ray diffraction (XRD) is a powerful technique to study the atomic crystal structure of bulk materials. This technique is based on the scattering of hard X-rays (photon energies of 5–25 keV) by the crystal lattice of the sample, which, in turn, provides information about the structure of nanoparticles, surfaces, interfaces and defects, and even average structural arrangement within liquids and at solid/liquid interfaces.[104] *In situ* XRD has been widely used to correlate X-ray diffraction and electrochemistry. Due to the high energy nature of the employed X-rays for XRD, easily able to pass through the electrolyte, performing successful *in situ* and *operando* experiments is easier than XAS and XPS. To be more surface-sensitive, grazing-incidence X-ray diffraction (GIXRD) is employed. In this configuration, the incident X-ray beam is directed onto a sample at a very low angle of incidence (usually < 1°), interacting only with the top few nanometers of the material.[105] However, the examples reported so far for PEC applications are very scarce, especially for solar fuel generation. Kang *et al.*[106] used *in situ* XRD, together with pole figures and HR-TEM, to investigate the formation process and the epitaxial properties of a Bi–WO_3 photoelectrode for PEC water oxidation. *In situ* XRD patterns revealed the process of self-assembly-oriented construction during the temperature-programmed calcination of the film, finding the preferential formation of monoclinic WO_3 nanocrystals at high temperatures ($T \geq 470$ °C) with dominant orientation along the (002) direction. Very recently, Wang *et al.*[107] have performed quasi *in situ* GIXRD to study the phase structure and chemical composition of a PdCu/TiO_2/Si photocathode surface before and after the Li-mediated PEC nitrogen reduction reaction (NRR). In GIXRD measurements, the incident angle was close to the critical angle for total reflection to increase the X-ray scattering signal.[104] By using this technique, the authors showed the appearance of a strong peak associated with $Li_2N_2O_3$ as the intermediate from the oxidation of Li or Li_3N under ambient air. Thus, these results revealed the formation of Li_3N from Li and N_2 during the PEC NRR, and also showed a higher stability of Li_3N and $Li_2N_2O_3$ in air than Li.[107]

X-ray scattering (XRS) is an all-atom technique that allows resolving structural parameters across the distance ranging from 10^{-11} m to 10^{-6} m,[108] whereas XRD describes the scattering of X-rays by a crystal lattice, and other X-ray scattering techniques investigate the atomic-, nano-, and micro-scale structure of less ordered matter, providing structural information of nanoparticles, defects, surface interfaces, and even the average structural arrangement within liquids or at liquid interfaces.[104]

Small-angle X-ray scattering (SAXS) can be used to study the morphological and structural changes in photoelectrodes and electrolytes, since it allows determining inhomogeneities ranging from the atomic to the nanometer length scales.[104,109] Thus, it allows probing local atomic structures and the formation of new phases on the photoelectrode surface.[109] More specifically, the grazing-incidence small-angle X-ray scattering (GISAXS) technique is used for studying the nano- and meso-scale evolution of surface structure in the range between 1 and 100 nanometers. This is a powerful technique for time-resolved *operando* studies during interface reactions, since GISAXS images can be obtained within seconds. Besides, this technique is insensitive to the crystal structure and it can be performed on any sufficiently planar interface, including amorphous and liquid substrates.[104]

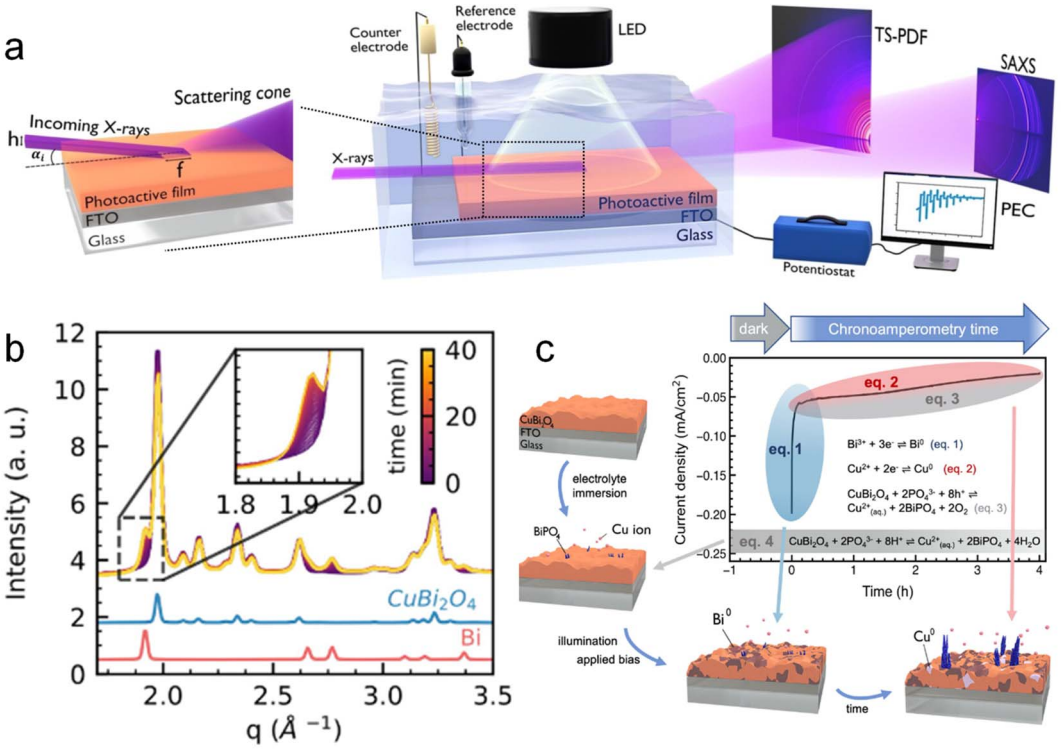

Fig. 10 (a) Schematic illustration of the multi-modal experimental set up: PEC properties of a photoactive thin film under illumination and when immersed in an electrolyte solution are probed using a potentiostat in a standard 3-electrode configuration. Two large-area X-ray detectors allow the simultaneous measurement of both TS and SAXS signals from the film surface in a grazing incidence geometry. (b) Time-resolved plot of the *operando* X-ray scattering signal collected from the surface of a $CuBi_2O_4$ electrode under illumination and applied constant bias (0.5 V *vs.* RHE). In the inset, a zoom into the 1.8–2.0 $Å^{-1}$ region highlights the formation of metallic Bi with time. (c) Schematic summary of the multiple reaction pathways and relative time scales determining the degradation of $CuBi_2O_4$ photocathodes before and during the chronoamperometric test. Copyright 2023. Reproduced with permission from Wiley. Adapted from ref. 109.

Koziej *et al.*[109] developed an *operando* grazing-incidence X-ray scattering approach to investigate the photocorrosion mechanisms and the evolution of structural modifications of a $CuBi_2O_4$ photoelectrode under illumination and applied bias. A scheme of the employed setup is shown in Fig. 10a. In this study, the total scattering (TS) measurements at the grazing-incidence angle were collected by using a high-energy X-ray probe and a large-area detector. Simultaneously, they also used a second large-area detector to collect the GISAXS signal, which was positioned at a different sample-to-detector distance than TS to acquire both signals at the same time. Specifically, by means of simultaneous and SAXS measurements, they found that $CuBi_2O_4$ electrodes quickly underwent a cathodic photocorrosion only few minutes after the beginning of the chronoamperometry, and a decrease of around one order of magnitude in the photocurrents. The authors ascribed these results to the formation of a segregating metallic Bi phase on the surface of the electrode, as shown in Fig. 10b, which significantly reduced the $CuBi_2O_4$ surface area in direct contact with the electrolyte. Besides, they observed an additional degradation process at slower timescales, associated with the formation of metallic Cu and subsequent dissolution in the electrolyte as a result of anionic photocorrosion and acidic dissolution. Both Cu^{2+} and Bi^{3+} ions released in solution interacted with the phosphate species from the electrolyte forming an insulating $BiPO_4$ layer on the surface of the electrode. This proposed mechanism is schematised in Fig. 10c. These results suggested avoiding the use of a phosphate buffer to prevent the unfavourable formation of $BiPO_4$. They also suggested the employment of a HER co-catalyst to avoid the reduction of $CuBi_2O_4$ to metallic Bi and Cu by quickly transferring the photogenerated electrons to the liquid phase.

Wide-Angle X-ray Scattering (WAXS) can provide signals from the catalyst at high diffraction angles, without any influence from the background or the PEC cell, and with a higher temporal resolution than SAXS.[104] Even though we were not able to find any work using *in situ* or *operando* WAXS in a PEC system, in 2020, Strasser *et al.*[110] were able to combine electrochemical OER measurements with *operando* WAXS, XAS data and theoretical calculations (*ab initio* molecular dynamics simulations and DFT) to track structural transformations during the activation of NiFe and CoFe LDH catalysts. These authors provided the first direct atomic-scale evidence for the oxidation of LDH from their as-prepared precursor state (α-phase) to the catalytically active states (deprotonated γ-phase) at a potential below the onset of the OER. The active γ-phases showed around 8% contractions of the lattice spacing, in both the in-plane lattice constant and the interlayer distance induced

Table 1 Most relevant technical aspects of XPS, XAS and XRD techniques

		XAS			
	XPS	Soft-XAS	Hard-XAS	XRD	XRS
Principle	Photoemission	Absorption		Diffraction	Scattering
Techniques	UHV-XPS NAP-XPS	Total electron yield Total fluorescence yield		Conventional XRD GIXRD	SAWS WAXS
Acquisition depth	1–10 nm	TEY: 10–20 nm TFY: 100 nm–100 μm		1–100 nm	1–100 nm
Detection limit	0.1–1.0% at.	10–100 g	10 μg–100 g	Depends on crystallinity of the sample	Depends on crystallinity and long range order of the sample
Advantages	Surface sensitive data acquisition dynamics (seconds) Quantitative information	Easier *in situ* cell configuration than for XPS	Ease of *in situ* and *operando* cell configuration Possibility of obtaining surface sensitive data (GIXRD, GISAWS)		
Disadvantages	*In situ* cell complexity (pressure conditions, membranes, *etc.*)	Complexity of surface sensitive measurements More qualitative than quantitative Data acquisition (minutes to hours)	More qualitative than quantitative Data acquisition (tens of minutes to hours)		
		Cell complexity in comparison to XRD and hard XAS	Difficult to decouple surface and bulk chemical changes	Only for crystalline samples	Complex data analysis (WAXS) SAWS (only for crystalline samples)

by the oxidation of the cations and the dynamics of the intercalated ions. This work demonstrates the high potential of WAXS for the understanding of the structural changes of electrocatalytic and surely photoelectrocatalytic materials under working conditions.

As extensively detailed in this study, (photo)electrochemical cell configurations and the information provided by XPS, XAS and XRD techniques vary significantly. In summary, XPS analyses the surface chemistry by detecting the electrons emitted from a material, revealing the elemental composition and chemical states of the top few nanometres. Furthermore, XAS, including both XANES and EXAFS, examines how a material absorbs X-rays to provide insights into local atomic structures, coordination environments, and oxidation states. Finally, XRD uses diffracted X-rays to determine the crystallographic structure, phase identification, and other structural properties of a material. Then, each technique serves specific purposes, where XPS focuses on surface analysis, XAS on local atomic environments and overall elemental composition and XRD on the crystal structure. Hence, due to these technical differences, the PEC cells for *in situ* and *operando* characterisation need to be designed precisely. Table 1 summarises the most relevant technical aspects of the analysed samples in the present study.

Apart from the above-detailed classic X-ray-based techniques (XPS, XAS and XRD), there are other configurations that are currently being developed at synchrotron facilities. Recently, several instruments have allowed performing different techniques using the same camera, known as multi-technique or multi-modal approach, such as NOTOS beamline in ALBA synchrotron, which enables performing XRD and XAS. Moreover, the 3Sbar beamline in ALBA, allows us to perform XPS and SAXS. Furthermore, in Max IV, XPS and IR are possible to be carried out. Besides, NAP XPS in synchrotron allows us to perform Auger yield XAS, which is surface sensitive. The main advantage of this multi-technique approach, summarized in the previous examples, relies on getting information from the exact same point in the sample and under exactly the same conditions. Moreover, there are other techniques such as tomography, for example available at Faxtor beamline in ALBA, that give a 3D image of the sample and could be well adapted to *in situ* and *operando* experiments. All these spectroscopies have demonstrated an enormous potential in the characterization of materials in general, and PEC systems in particular, under working conditions.

The future of XPS, XAS, and XRD techniques for *in situ* and *operando* characterisation of photoelectrodes is highly promising, where significant advancements are expected. These advances include the development of ambient pressure and time-resolved XPS for realistic and dynamic surface studies, improved resolution and sensitivity in XAS through next-generation synchrotron sources as well as the integration of XAS with neutron scattering for comprehensive structural insights. Additionally, real-time and rapid XRD measurements, along with X-ray tomography, will enhance the understanding of structural changes and phase distribution in photoelectrodes. Additionally, the synergy of multi-modal techniques, as detailed above, and the use of artificial intelligence for data analysis will provide a more comprehensive characterization, driving the discovery and optimization of new materials. Therefore, the enhanced operational conditions during

measurements will lead to more precise and relevant studies, ultimately contributing to the development of more efficient and durable photoelectrocatalytic materials.

Conclusions

The present work summarized the most relevant *in situ* and *operando* X-ray studies in PEC systems, demonstrating the strength and potential of these spectroscopies for the characterisation of PEC materials under working conditions. Specifically, this work is focused on *operando* and *in situ* XPS, XAS and XRD techniques, trying to remark the recent progress using these techniques for elucidating the structural, chemical, compositional and electronic properties of photoelectrocatalytic materials and interfaces. Moreover, this work provides technical guidance for adequately conducting these complex experiments, focusing on the possibilities of the analysed techniques, cell designs and more relevant results.

It is apparent that many of the above-discussed X-ray-based techniques have benefited from the developments and upgrades of different synchrotron beamlines. Accordingly, we believe that the success of the *in situ* and *operando* characterisation is currently mainly limited by the PEC cell engineering, where film and electrolyte thickness, as well as photoelectrode disposition, play a key role. In this context, making the cell designs publicly available will greatly benefit the field and will promote a deep understanding of PEC processes aiming to design more efficient and stable photoelectrodes for solar-driven fuel production and value-added photoelectrosynthesised compounds.

Data availability

This manuscript is a review article, and as such, it synthesizes and discusses results and findings from previously published studies that have undergone rigorous peer-review and have been published in reputable scientific journals. All data, results, and figures included in this review are sourced from these original publications. We have obtained all necessary permissions for the reproduction of figures and any other content from these studies. Proper citations and acknowledgments are provided to ensure that credit is given to the original authors and sources. No new primary data were generated or analysed in the preparation of this manuscript. Should any additional information be required regarding the sources or permissions for the reproduced content, it is available upon request from the corresponding author.

Conflicts of interest

There are no conflicts to declare.

Acknowledgements

The project that gave rise to these results received the support of a fellowship from "la Caixa" Foundation (ID 100010434). The fellowship code is LCF/BQ/PR23/11980046. Additionally, this work has received financial support through the projects SOL-FUTURE (PLEC2021-007906), TED2021-130173B-C41 and TED2021-129999A-C33 funded by MCIN/AEI/10.13039/501100011033 and the European Union NextGenerationEU/PRTR. Also, the authors acknowledge financial support from the EU FETPROACT-EIC-07-2020 programme (HYSOLCHEM 101017928). M. Barawi acknowledges NovaCO_2 project (PID2020-118593RB-C22) and the RYC2022-038157-I Grant funded by MCIN/AEI/10.13039/501100011033. L. Collado acknowledges the project ARMONIA (PID2020-119125RJ-I00) funded by MICIU/AEI/10.13039/501100011033. I. J. Villar-García would like to acknowledge the project OSMIBatt (CNS2022-135285) funded by MCIN/AEI/10.13039/501100011033 and European Union NextGenerationEU. F. E. Oropeza thanks to MINECO and European NextGenerationEU/PRTR Fund for the Ramón y Cajal contract (RyC2021-034254-I).

References

1 J. Li and N. Wu, *Catal. Sci. Technol.*, 2015, **5**, 1360–1384.
2 S. D. Tilley, *Adv. Energy Mater.*, 2019, **9**, 1802877.
3 B. Tumas, J. Dempsey, T. Mollouk, S. Ardo, K. Bren, A. Rappe, W. Shaw, H. Abruna, H. Atwater, K. Ayers, C. Berlinguette, J. Concepcion, V. Cooper, D. Esposito, J. Gregorie, L. Hammarstrom, S. Haussener, F. Houle, S. Linic, H. Shafaat, Y. Shao-Horn, W. Smith, Y. Surendranath, D. Tiede and J. Yang, *Report of the Basic Energy Sciences Roundtable on Liquid Solar Fuels*, 2019.
4 A. Sharma, T. Longden, K. Catchpole and F. J. Beck, *Energy Environ. Sci.*, 2023, **16**, 4486–4501.
5 G. Segev, J. Kibsgaard, C. Hahn, Z. J. Xu, W.-H. Cheng, T. G. Deutsch, C. Xiang, J. Z. Zhang, L. Hammarström, D. G. Nocera, A. Z. Weber, P. Agbo, T. Hisatomi, F. E. Osterloh, K. Domen, F. F. Abdi, S. Haussener, D. J. Miller, S. Ardo, P. C. McIntyre, T. Hannappel, S. Hu, H. Atwater, J. M. Gregoire, M. Z. Ertem, I. D. Sharp, K.-S. Choi, J. S. Lee, O. Ishitani, J. W. Ager, R. R. Prabhakar, A. T. Bell, S. W. Boettcher, K. Vincent, K. Takanabe, V. Artero, R. Napier, B. R. Cuenya, M. T. M. Koper, R. Van De Krol and F. Houle, *J. Phys. D Appl. Phys.*, 2022, **55**, 323003.
6 H. Liang, Z. Yan and G. Zeng, *Inorganics*, 2022, **11**, 16.
7 R. Yalavarthi, O. Henrotte, A. Minguzzi, P. Ghigna, D. A. Grave and A. Naldoni, *MRS Energy Sustain.*, 2020, **7**, 37.
8 A. Gurlo and R. Riedel, *Angew. Chem., Int. Ed.*, 2007, **46**, 3826–3848.
9 E. Pastor, Z. Lian, L. Xia, D. Ecija, J. R. Galán-Mascarós, S. Barja, S. Giménez, J. Arbiol, N. López and F. P. García de Arquer, *Nat. Rev. Chem*, 2024, **8**, 159–178.
10 R. R. Rao, S. Corby, A. Bucci, M. García-Tecedor, C. A. Mesa, J. Rossmeisl, S. Giménez, J. Lloret-Fillol, I. E. L. Stephens and J. R. Durrant, *J. Am. Chem. Soc.*, 2022, **144**, 7622–7633.
11 Y. AlSalka, S. Schwabe, J. Geweke, G. Ctistis and H. Wackerbarth, *Energy Technol.*, 2022, **11**, 2200788.
12 R. Arcas, D. Cardenas-Morcoso, M. C. Spadaro, M. García-Tecedor, C. A. Mesa, J. Arbiol, F. Fabregat-Santiago, S. Giménez and E. Mas-Marzá, *Sol. RRL*, 2022, **6**, 2200132.

13 A. Venugopal, R. Kas, K. Hau and W. A. Smith, *J. Am. Chem. Soc.*, 2021, **143**, 18581–18591.
14 M. García-Tecedor, M. Barawi, A. García-Eguizábal, M. Gomez-Mendoza, F. E. Oropeza, G. Gorni, A. Cibotaru, M. Liras and V. A. de la Peña O'Shea, *Sol. RRL*, 2024, **8**, 2301069.
15 A. O. Alvarez, M. García-Tecedor, L. Montañés, E. Mas-Marzá, S. Giménez and F. Fabregat-Santiago, *Sol. RRL*, 2022, **6**, 2200826.
16 Advanced Certificate in Powder Diffraction on the Web, *Course Material Master Index*, School of Crystallography, Birkbeck College, **https://pd.chem.ucl.ac.uk/pd/welcome.htm**.
17 J. Noguera-Gómez, M. García-Tecedor, J. F. Sánchez-Royo, L. M. Valencia Liñán, M. de la Mata, M. Herrera-Collado, S. I. Molina, R. Abargues and S. Giménez, *ACS Appl. Energy Mater.*, 2021, **4**, 5255–5264.
18 B. Moss, K. L. Svane, D. Nieto-Castro, R. R. Rao, S. B. Scott, C. Tseng, M. Sachs, A. Pennathur, C. Liang, L. I. Oldham, E. Mazzolini, L. Jurado, G. Sankar, S. Parry, V. Celorrio, J. M. Dawlaty, J. Rossmeisl, J. R. Galán-Mascarós, I. E. L. Stephens and J. R. Durrant, *J. Am. Chem. Soc.*, 2024, **146**, 8915–8927.
19 X. Ding, D. Liu, P. Zhao, X. Chen, H. Wang, F. E. Oropeza, G. Gorni, M. Barawi, M. García-Tecedor, V. A. de la Peña O'Shea, J. P. Hofmann, J. Li, J. Kim, S. Cho, R. Wu and K. H. L. Zhang, *Nat. Commun.*, 2024, **15**, 5336.
20 S. Corby, M.-G. Tecedor, S. Tengeler, C. Steinert, B. Moss, C. A. Mesa, H. F. Heiba, A. A. Wilson, B. Kaiser, W. Jaegermann, L. Francàs, S. Gimenez and J. R. Durrant, *Sustainable Energy Fuels*, 2020, **4**, 5024–5030.
21 Z. Zhang, H. Nagashima and T. Tachikawa, *Angew. Chem., Int. Ed.*, 2020, **59**, 9047–9054.
22 H. Wang, Y. Wang, Y. Lin, X. Huang, M. García-Tecedor, V. A. de la Peña O'Shea, C. Murrill, V. K. Lazarov, F. E. Oropeza and K. H. L. Zhang, *ACS Appl. Mater. Interfaces*, 2023, **15**, 28739–28746.
23 T. Lopes, P. Dias, L. Andrade and A. Mendes, *Sol. Energy Mater. Sol. Cells*, 2014, **128**, 399–410.
24 *Surface and Interfacial Aspects of Biomedical Polymer*, ed. J. D. Andrade, Plenum Press, New York, 1985.
25 F. A. Stevie and C. L. Donley, *J. Vac. Sci. Technol.*, 2020, **38**, 063204.
26 D. F. Ogletree, H. Bluhm, G. Lebedev, C. S. Fadley, Z. Hussain and M. Salmeron, *Rev. Sci. Instrum.*, 2002, **73**, 3872–3877.
27 J. Schnadt, J. Knudsen and N. Johansson, *J. Phys.: Condens.Matter*, 2020, **32**, 413003.
28 M. Favaro, L. Artiglia and B. S. Mun, *J. Phys. D Appl. Phys.*, 2022, **55**, 060201.
29 J.-J. Velasco-Vélez, L. J. Falling, D. Bernsmeier, M. J. Sear, P. C. J. Clark, T.-S. Chan, E. Stotz, M. Hävecker, R. Kraehnert, A. Knop-Gericke, C.-H. Chuang, D. E. Starr, M. Favaro and R. V Mom, *J. Phys. D Appl. Phys.*, 2021, **54**, 124003.
30 A. Kolmakov, D. A. Dikin, L. J. Cote, J. Huang, M. K. Abyaneh, M. Amati, L. Gregoratti, S. Günther and M. Kiskinova, *Nat. Nanotechnol.*, 2011, **6**, 651–657.
31 R. S. Weatherup, *Top. Catal.*, 2018, **61**, 2085–2102.
32 P. Leidinger, J. Kraus, T. Kratky, P. Zeller, T. O. Menteş, F. Genuzio, A. Locatelli and S. Günther, *J. Phys. D Appl. Phys.*, 2021, **54**, 234001.
33 S. Axnanda, E. J. Crumlin, B. Mao, S. Rani, R. Chang, P. G. Karlsson, M. O. M. Edwards, M. Lundqvist, R. Moberg, P. Ross, Z. Hussain and Z. Liu, *Sci. Rep.*, 2015, **5**, 9788.
34 A. Klyushin, M. Ghosalya, E. Kokkonen, C. Eads, R. Jones, N. Nalajala, C. S. Gopinath and S. Urpelainen, *J. Synchrotron Radiat.*, 2023, **30**, 613–619.
35 M. Favaro, P. C. J. Clark, M. J. Sear, M. Johansson, S. Maehl, R. van de Krol and D. E. Starr, *Surf. Sci.*, 2021, **713**, 121903.
36 A. Benayad, J. E. Morales-Ugarte, C. C. Santini and R. Bouchet, *J. Phys. Chem. A*, 2021, **125**, 1069–1081.
37 H. Sezen and S. Suzer, *Thin Solid Films*, 2013, **534**, 1–11.
38 J. E. Demuth, W. J. Thompson, N. J. DiNardo and R. Imbihl, *Phys. Rev. Lett.*, 1986, **56**, 1408–1411.
39 S. Teich, S. Grafström and L. M. Eng, *Surf. Sci.*, 2004, **552**, 77–84.
40 H. Sezen, E. Ozbay and S. Suzer, *Appl. Surf. Sci.*, 2014, **323**, 25–30.
41 J. E. Demuth, B. N. J. Persson and A. J. Schell-Sorokin, *Phys. Rev. Lett.*, 1983, **51**, 2214–2217.
42 H. Sezen and S. Suzer, *Surf. Sci.*, 2010, **604**, L59–L62.
43 O. Ö. Ekiz, K. Mizrak and A. Dâna, *ACS Nano*, 2010, **4**, 1851–1860.
44 F. E. Oropeza, B. T. Feleki, K. H. L. Zhang, E. J. M. Hensen and J. P. Hofmann, *ACS Appl. Energy Mater.*, 2019, **2**, 6866–6874.
45 L. Gao, Y. Cui, R. H. J. Vervuurt, D. van Dam, R. P. J. van Veldhoven, J. P. Hofmann, A. A. Bol, J. E. M. Haverkort, P. H. L. Notten, E. P. A. M. Bakkers and E. J. M. Hensen, *Adv. Funct. Mater.*, 2016, **26**, 679–686.
46 Ø. Dahl, M. F. Sunding, V. Killi, I.-H. Svenum, M. Grandcolas, M. Andreassen, O. Nilsen, A. Thøgersen, I. J. T. Jensen and A. Chatzitakis, *ACS Catal.*, 2023, **13**, 11762–11770.
47 X. Zhang and S. Ptasinska, *Appl. Surf. Sci.*, 2020, **516**, 146127.
48 X. Zhang and S. Ptasinska, *Phys. Chem. Chem. Phys.*, 2015, **17**, 3909–3918.
49 X. Zhang and S. Ptasinska, *Sci. Rep.*, 2016, **6**, 24848.
50 R. Subbaraman, D. Tripkovic, D. Strmcnik, K.-C. Chang, M. Uchimura, A. P. Paulikas, V. Stamenkovic and N. M. Markovic, *Science*, 2011, **334**, 1256–1260.
51 N. Dubouis and A. Grimaud, *Chem. Sci.*, 2019, **10**, 9165–9181.
52 M. J. Jackman, A. G. Thomas and C. Muryn, *J. Phys. Chem. C*, 2015, **119**, 13682–13690.
53 S. Porsgaard, P. Jiang, F. Borondics, S. Wendt, Z. Liu, H. Bluhm, F. Besenbacher and M. Salmeron, *Angew. Chem., Int. Ed.*, 2011, **50**, 2266–2269.

54 V. Mansfeldova, M. Zlamalova, H. Tarabkova, P. Janda, M. Vorokhta, L. Piliai and L. Kavan, *J. Phys. Chem. C*, 2021, **125**, 1902–1912.
55 M. F. Lichterman, S. Hu, M. H. Richter, E. J. Crumlin, S. Axnanda, M. Favaro, W. Drisdell, Z. Hussain, T. Mayer, B. S. Brunschwig, N. S. Lewis, Z. Liu and H.-J. Lewerenz, *Energy Environ. Sci.*, 2015, **8**, 2409–2416.
56 M. Favaro, I. Y. Ahmet, P. C. J. Clark, F. F. Abdi, M. J. Sear, R. van de Krol and D. E. Starr, *J. Phys. D Appl. Phys.*, 2021, **54**, 164001.
57 P. Amann, D. Degerman, M.-T. Lee, J. D. Alexander, M. Shipilin, H.-Y. Wang, F. Cavalca, M. Weston, J. Gladh, M. Blom, M. Björkhage, P. Löfgren, C. Schlueter, P. Loemker, K. Ederer, W. Drube, H. Noei, J. Zehetner, H. Wentzel, J. Åhlund and A. Nilsson, *Rev. Sci. Instrum.*, 2019, **90**, 103102.
58 J. Knudsen, T. Gallo, V. Boix, M. D. Strømsheim, G. D'Acunto, C. Goodwin, H. Wallander, S. Zhu, M. Soldemo, P. Lömker, F. Cavalca, M. Scardamaglia, D. Degerman, A. Nilsson, P. Amann, A. Shavorskiy and J. Schnadt, *Nat. Commun.*, 2021, **12**, 6117.
59 D. Ketenoglu, *X-Ray Spectrom.*, 2022, **51**, 422–443.
60 *X-Ray Absorption and X-Ray Emission Spectroscopy*, ed. J. A. Van Bokhoven and C. Lamberti, Wiley, 2016.
61 N. S. Genz, A. Kallio, F. Meirer, S. Huotari and B. M. Weckhuysen, *Chem.: Methods*, 2024, **4**, e202300027.
62 R. Koningsberger and D. C. Prins, *X-Ray Absorption: Principles, Applications, Techniques of EXAFS*, SEXAFS and XANES, 1987.
63 S. L. M. Schroeder, G. D. Moggridge, T. Rayment and R. M. Lambert, *J. Mol. Catal. A: Chem.*, 1997, **119**, 357–365.
64 K. Nakanishi and T. Ohta, *Surf. Interface Anal.*, 2012, **44**, 784–788.
65 W.-S. Yoon, M. Balasubramanian, K. Y. Chung, X.-Q. Yang, J. McBreen, C. P. Grey and D. A. Fischer, *J. Am. Chem. Soc.*, 2005, **127**, 17479–17487.
66 P. Zimmermann, S. Peredkov, P. M. Abdala, S. DeBeer, M. Tromp, C. Müller and J. A. van Bokhoven, *Coord. Chem. Rev.*, 2020, **423**, 213466.
67 J. Deng, Q. Zhang, X. Lv, D. Zhang, H. Xu, D. Ma and J. Zhong, *ACS Energy Lett.*, 2020, **5**, 975–993.
68 M. A. Soldatov, P. V. Medvedev, V. Roldugin, I. N. Novomlinskiy, I. Pankin, H. Su, Q. Liu and A. V. Soldatov, *Nanomaterials*, 2022, **12**, 839.
69 N. Rossetti, A. Ugolotti, C. Cometto, V. Celorrio, G. Dražić, C. Di Valentin and L. Calvillo, *J. Mater. Chem. A*, 2024, **12**, 6652–6662.
70 P. Ren, T. Zhang, N. Jain, H. Y. V. Ching, A. Jaworski, G. Barcaro, S. Monti, J. Silvestre-Albero, V. Celorrio, L. Chouhan, A. Rokicińska, E. Debroye, P. Kuśtrowski, S. Van Doorslaer, S. Van Aert, S. Bals and S. Das, *J. Am. Chem. Soc.*, 2023, **145**, 16584–16596.
71 C.-W. Tung, C.-H. Hou, H.-T. Lin, Y. Zheng, Y.-P. Huang, Y.-F. Liao, J.-J. Shiue and H. M. Chen, *Sol. RRL*, 2020, **4**, 2000028.
72 J. Wang, X. Ge, L. Shao, J. Zhang, D. Peng, G. Zou, H. Hou, W. Deng, S. Xu, X. Ji and W. Zhang, *Mater. Today Energy*, 2020, **17**, 100436.
73 J. Zheng, Y. Lyu, J.-P. Veder, B. Johannessen, R. Wang, R. De Marco, A. Huang, S. P. Jiang and S. Wang, *J. Phys. Chem. C*, 2021, **125**, 23041–23049.
74 Z. H. Lu, T. K. Sham, M. Vos, A. Bzowski, I. V. Mitchell and P. R. Norton, *Phys. Rev. B: Condens. Matter Mater. Phys.*, 1992, **45**, 8811–8814.
75 J. Zheng, Y. Lyu, A. Huang, B. Johannessen, X. Cao, S. P. Jiang and S. Wang, *Chin. J. Catal.*, 2023, **45**, 141–151.
76 M. Suksomboon, K. Kongsawatvoragul, S. Duangdangchote and M. Sawangphruk, *ACS Omega*, 2021, **6**, 20804–20811.
77 H. Pang, X. Li, Q. Zhao, H. Xue, W.-Y. Lai, Z. Hu and W. Huang, *Nano Energy*, 2017, **35**, 138–145.
78 S. Kalasina, P. Pattanasattayavong, M. Suksomboon, N. Phattharasupakun, J. Wutthiprom and M. Sawangphruk, *Chem. Commun.*, 2017, **53**, 709–712.
79 J. M. Yu, J. Lee, Y. S. Kim, J. Song, J. Oh, S. M. Lee, M. Jeong, Y. Kim, J. H. Kwak, S. Cho, C. Yang and J.-W. Jang, *Nat. Commun.*, 2020, **11**, 5509.
80 P. Iamprasertkun, A. Krittayavathananon, A. Seubsai, N. Chanlek, P. Kidkhunthod, W. Sangthong, S. Maensiri, R. Yimnirun, S. Nilmoung, P. Pannopard, S. Ittisanronnachai, K. Kongpatpanich, J. Limtrakul and M. Sawangphruk, *Sci. Rep.*, 2016, **6**, 37560.
81 J. Li, H. Chen, C. A. Triana and G. R. Patzke, *Angew. Chem., Int. Ed.*, 2021, **60**, 18380–18396.
82 T. H. Jeon, G. Moon, H. Park and W. Choi, *Nano Energy*, 2017, **39**, 211–218.
83 C. A. Mesa, E. Pastor and L. Francàs, *Curr. Opin. Electrochem.*, 2022, **35**, 101098.
84 M. Li, J. Deng, A. Pu, P. Zhang, H. Zhang, J. Gao, Y. Hao, J. Zhong and X. Sun, *J. Mater. Chem. A*, 2014, **2**, 6727.
85 C. A. Mesa, M. Sachs, E. Pastor, N. Gauriot, A. Merryweather, M. A. Gomez-Gonzalez, K. Ignatyev, S. Giménez, R. Rao, J. R. Durrant and R. Pandya, *Nat. Commun.*, 2024, **15**, 3904.
86 A. Braun, K. Sivula, D. K. Bora, J. Zhu, L. Zhang, M. Grätzel, J. Guo and E. C. Constable, *J. Phys. Chem. C*, 2012, **116**, 16870–16875.
87 F. Malara, M. Fracchia, H. Kmentová, R. Psaro, A. Vertova, D. Oliveira de Souza, G. Aquilanti, L. Olivi, P. Ghigna, A. Minguzzi and A. Naldoni, *ACS Catal.*, 2020, **10**, 10476–10487.
88 Y. Liu, C. Wei, C. K. Ngaw, Y. Zhou, S. Sun, S. Xi, Y. Du, J. S. C. Loo, J. W. Ager and Z. J. Xu, *ACS Appl. Energy Mater.*, 2018, **1**, 814–821.
89 H.-W. Chang, Y. Fu, W.-Y. Lee, Y.-R. Lu, Y.-C. Huang, J.-L. Chen, C.-L. Chen, W. C. Chou, J.-M. Chen, J.-F. Lee, S. Shen and C.-L. Dong, *Nanotechnology*, 2018, **29**, 064002.
90 Y. R. Lu, Y. F. Wang, H. W. Chang, Y. C. Huang, J. L. Chen, C. L. Chen, Y. C. Lin, Y. G. Lin, W. F. Pong, T. Ohigashi, N. Kosugi, C. H. Kuo, W. C. Chou and C. L. Dong, *Sol. Energy Mater. Sol. Cells*, 2020, **209**, 110469.
91 Y. Uemura, A. S. M. Ismail, S. H. Park, S. Kwon, M. Kim, H. Elnaggar, F. Frati, H. Wadati, Y. Hirata, Y. Zhang,

K. Yamagami, S. Yamamoto, I. Matsuda, U. Halisdemir, G. Koster, C. Milne, M. Ammann, B. M. Weckhuysen and F. M. F. de Groot, *J. Phys. Chem. Lett.*, 2022, **13**, 4207–4214.

92 A. Braun, Y. Hu, F. Boudoire, D. K. Bora, D. D. Sarma, M. Grätzel and C. M. Eggleston, *Catal. Today*, 2016, **260**, 72–81.

93 A. S. M. Ismail, I. Garcia-Torregrosa, J. C. Vollenbroek, L. Folkertsma, J. G. Bomer, T. Haarman, M. Ghiasi, M. Schellhorn, M. Nachtegaal, M. Odijk, A. van den Berg, B. M. Weckhuysen and F. M. F. de Groot, *ACS Catal.*, 2021, **11**, 12324–12335.

94 L. Xi, C. Schwanke, D. Zhou, D. Drevon, R. van de Krol and K. M. Lange, *Dalton Trans.*, 2017, **46**, 15719–15726.

95 L. Xi, F. Wang, C. Schwanke, F. F. Abdi, R. Golnak, S. Fiechter, K. Ellmer, R. van de Krol and K. M. Lange, *J. Phys. Chem. C*, 2017, **121**, 19668–19676.

96 S. P. Cramer, F. M. F. de Groot, Y. Ma, C. T. Chen, F. Sette, C. A. Kipke, D. M. Eichhorn, K. Chan, W. H. Armstrong, E. Libby, G. Christou, J. C. Fuggle, S. Brooker, V. McKee and O. C. Mullins, *J. Am. Chem. Soc.*, 2002, **113**, 7937–7940.

97 L. Xi, C. Schwanke, J. Xiao, F. F. Abdi, I. Zaharieva and K. M. Lange, *J. Phys. Chem. C*, 2017, **121**, 12003–12009.

98 C. Schwanke, L. Xi and K. M. Lange, *J. Synchrotron Radiat.*, 2016, **23**, 1390–1394.

99 L. Xi, M. Schellenberger, R. F. Praeg, D. Gao, D. Drevon, P. Plate, P. Bogdanoff, R. van de Krol and K. M. Lange, *ACS Appl. Energy Mater.*, 2019, **2**, 4126–4134.

100 R. A. Vicente, S. P. Raju, H. V. N. Gomes, I. T. Neckel, H. C. N. Tolentino and P. S. Fernández, *Anal. Chem.*, 2023, **95**, 16144–16152.

101 R. A. Vicente, I. T. Neckel, S. K. R. S. Sankaranarayanan, J. Solla-Gullon and P. S. Fernández, *ACS Nano*, 2021, **15**, 6129–6146.

102 P. Jiang, J.-L. Chen, F. Borondics, P.-A. Glans, M. W. West, C.-L. Chang, M. Salmeron and J. Guo, *Electrochem. Commun.*, 2010, **12**, 820–822.

103 P. Sedigh Rahimabadi, M. Khodaei and K. R. Koswattage, *X-Ray Spectrom.*, 2020, **49**, 348–373.

104 O. M. Magnussen, J. Drnec, C. Qiu, I. Martens, J. J. Huang, R. Chattot and A. Singer, *Chem. Rev.*, 2024, **124**, 629–721.

105 P. Müller-Buschbaum, in *Applications of Synchrotron Light to Scattering and Diffraction in Materials and Life Sciences*, Springer Berlin Heidelberg, Berlin, 2009, pp. 61–89.

106 J. Y. Zheng, A. U. Pawar, C. W. Kim, Y. J. Kim and Y. S. Kang, *Appl. Catal., B*, 2018, **233**, 88–98.

107 X. Zhang, Y. Lyu, H. Zhou, J. Zheng, A. Huang, J. Ding, C. Xie, R. De Marco, N. Tsud, V. Kalinovych, S. P. Jiang, L. Dai and S. Wang, *Adv. Mater.*, 2023, **35**, 2211894.

108 K. L. Mulfort, A. Mukherjee, O. Kokhan, P. Du and D. M. Tiede, *Chem. Soc. Rev.*, 2013, **42**, 2215–2227.

109 D. Derelli, F. Caddeo, K. Frank, K. Krötzsch, P. Ewerhardt, M. Krüger, S. Medicus, L. Klemeyer, M. Skiba, C. Ruhmlieb, O. Gutowski, A. Dippel, W. J. Parak, B. Nickel and D. Koziej, *Angew. Chem., Int. Ed.*, 2023, **62**, e202307948.

110 F. Dionigi, Z. Zeng, I. Sinev, T. Merzdorf, S. Deshpande, M. B. Lopez, S. Kunze, I. Zegkinoglou, H. Sarodnik, D. Fan, A. Bergmann, J. Drnec, J. F. de Araujo, M. Gliech, D. Teschner, J. Zhu, W.-X. Li, J. Greeley, B. R. Cuenya and P. Strasser, *Nat. Commun.*, 2020, **11**, 2522.